

# AGN proximity zone fossils and the delayed recombination of metal lines

Benjamin D. Oppenheimer<sup>1</sup>, Joop Schaye<sup>1</sup>

<sup>1</sup> *Leiden Observatory, Leiden University, PO Box 9513, 2300 RA Leiden, the Netherlands*

2 December 2024

## ABSTRACT

We model the time-dependent evolution of metal-enriched intergalactic and circumgalactic gas exposed to the fluctuating radiation field from an active galactic nucleus (AGN). We consider diffuse gas densities ( $n_{\text{H}} = 10^{-5} - 10^{-3} \text{cm}^{-3}$ ) exposed to the extra-galactic background (EGB) and initially in thermal equilibrium ( $T \sim 10^4 - 10^{4.5}$  K). Once the proximate AGN field turns on, additional photo-ionisation rapidly ionises the H I and metals. The enhanced AGN radiation field turns off after a typical AGN lifetime ( $\tau_{\text{AGN}} = 1 - 20$  Myr) and the field returns to the EGB intensity, but the metals remain out of ionisation equilibrium for timescales that can significantly exceed  $\tau_{\text{AGN}}$ . We define this phase as the AGN proximity zone “fossil” phase and show that high ionisation stages (e.g. O VI, Ne VIII, Mg X) are in general enhanced, while the abundances of low ions (e.g. C IV, O IV, Mg II) are reduced. In contrast, H I re-equilibrates rapidly ( $\ll \tau_{\text{AGN}}$ ) owing to its low neutral fraction at diffuse densities. We demonstrate that metal column densities of intervening gas observed in absorption in quasar sight lines are significantly affected by delayed recombination for a wide range of densities, metallicities, AGN strengths, AGN lifetimes, and AGN duty cycles. We model the exceptionally strong  $z = 0.9$  Ne VIII absorbers observed by Tripp et al. (2011) as arising in a possible fossil zone or near a recently turned-on AGN and we demonstrate that at low redshift even moderate-strength AGN that are off for 90% of the time could significantly enhance the high-ion metal columns in the circumgalactic media of galaxies observed without active AGN. Fossil proximity zones may be particularly important during the quasar era,  $z \sim 2 - 5$ . Indeed, we demonstrate that at these redshifts a large fraction of the metal-enriched intergalactic medium may consist of out-of-equilibrium fossil zones. AGN proximity zone fossils allow a whole new class of non-equilibrium solutions that may be applicable to a large fraction of observed metal absorbers and which could potentially change the inferred physical conditions and masses of diffuse gases.

**Key words:** atomic processes; plasmas; galaxies: formation; intergalactic medium; quasars: absorption lines; Seyfert; cosmology: theory;

## 1 INTRODUCTION

Active galactic nuclei (AGN) provide the majority of photons capable of ionising intergalactic hydrogen over most of the age of the Universe (e.g. Shull et al. 1999; Haardt & Madau 2012). Some of the most commonly observed metal absorption lines in the intergalactic medium (IGM), including C IV and O VI, have ionisation potentials at extreme UV (EUV) energies where their main photo-ionising sources are AGN. The mean free paths of ionising photons with energies greater than 1 Rydberg are long enough to warrant the assumption that the ionising extra-galactic background (EGB) is uniform in its spatial distribution (e.g. Zuo 1992). The main criterion for this assumption is that the

mean free paths of photons are longer than the clustering length of photo-ionising sources (e.g. Faucher-Giguère et al. 2009).

This assumption obviously breaks down near sources of ionising radiation. Particularly notable are the proximity zones of QSOs, where the locally generated ionising radiation at EUV energies may exceed the EGB by orders of magnitude. The simple nature of hydrogen, having only two ionisation states, allows an elegant relationship where, in ionisation equilibrium, the neutral fraction scales in inverse linear proportion to the ionisation field strength if hydrogen is photo-ionised. A dramatic example of this are the proximity zones of high- $z$  quasars, where

the Ly $\alpha$  forest absorption is significantly reduced by the enhanced AGN radiation field as the QSO is approached (e.g. Carswell et al. 1987; Bajtlik et al. 1988; Scott et al. 2000; Bolton & Haehnelt 2007). QSO pairs can probe the transverse proximity effect in which the background QSO line of sight intersects the foreground QSO proximity zone, where the radiation field is increased by orders of magnitude compared to the typical EGB (e.g. Jakobsen et al. 2003; Schirber et al. 2004; Hennawi et al. 2006; Gonçalves et al. 2008).

Metal absorption also reflects the effects of increased ionisation in quasar proximity zones. Proximate absorbers are often defined as being within 5000 km s<sup>-1</sup> of the QSO velocity along the line of sight, and show some distinct signatures such as O VI absorption with little or no H I absorption (e.g. Tripp et al. 2008). Gonçalves et al. (2008) observe unique metal-line systems at  $z \sim 2.5$  in transverse proximate zones with an ionisation enhancement of 10-200 $\times$ , where O VI is enhanced and C IV is weakened. These signatures suggest that enhanced photo-ionisation affects metal lines, but in a different way than hydrogen. The multiple ionisation levels of heavy elements makes the response to increased ionisation more complex: metal ion fractions of order unity are possible at diffuse IGM densities (i.e. much higher than H I fractions); plus these fractions are not a monotonic function of density or temperature like that of H I, but instead peak at a preferred density or temperature for an intermediate ionisation state. In the case of an increased ionisation field, the peak ionisation fraction for a metal species will move in linear proportion with the photo-ionisation rate to higher density if the species is photo-ionised and in equilibrium.

Another difference between hydrogen and metal species is the timescale that it takes each to achieve ionisation equilibrium when a proximate AGN turns on and off. The ionisation timescales, relevant for the AGN turn on, are longer for metal species with higher ionisation potentials, because fewer ionising photons are produced by the AGN at these higher energies. However, the more important difference is the longer timescales metals take to reach ionisation equilibrium after the AGN turns off. Although most metal species have shorter recombination timescales,  $\tau_{\text{rec}}$ , than H II, the relevant timescale to achieve equilibrium is  $\tau_{\text{rec}}$  times the equilibrium ionisation fraction of the recombined species. For example, at typical warm ( $T \sim 10^4$  K) IGM densities of the Ly $\alpha$  forest ( $n_{\text{H}} \sim 10^{-4}$  cm<sup>-3</sup>),  $\tau_{\text{rec,HII}} \sim 10^9$  yr, but the H I ionisation fraction,  $f_{\text{HI}}$ , is  $\sim 10^{-4}$ ; hence the equilibration timescale is only  $\sim 10^5$  yr, because hydrogen only has to recombine to a very low neutral fraction to achieve equilibrium. Metal-line species like C IV and O VI have recombination timescales that are  $\gtrsim 10^7$  yr at similar warm IGM densities, but typical ionisation fractions much closer to unity. Therefore, timescales to recombine to equilibrium are also  $\gtrsim 10^7$  yr – much longer than for H I. Furthermore, the existence of multiple ionisation states for metals means that there are a series of ions to recombine through, and hence multiple recombination timescales, further extending the total equilibration timescale.

AGN proximity zone fossils are defined as proximity zones in which the AGN has turned off, but ionisation equilibrium has not yet been achieved. The fossil lifetime can last much longer than the AGN-on

phase, which is often calculated to be  $\sim 10^6 - 10^8$  yr (e.g. Haiman & Hui 2001; Martini & Weinberg 2001; Jakobsen et al. 2003; Schirber et al. 2004; Hopkins et al. 2006; Gonçalves et al. 2008). In this work, we use the non-equilibrium code introduced in Oppenheimer & Schaye (2013) to follow the ionisation and temperature evolution of metal-enriched gas subjected to a variable ionisation field owing to an AGN. We consider several situations where the fossil stage lasts as long as, and sometimes much longer than the AGN phase. We predict the absorption line signatures of these fossil zones, and compare them to some recent observational results. We focus on diffuse gas with hydrogen numbers densities  $n_{\text{H}} = 10^{-5} - 10^{-3}$  cm<sup>-3</sup> (i.e.  $\rho/\langle\rho\rangle \sim (50 - 5000) \times (1+z)^{-3}$ ), initially at the equilibrium temperature where cooling balances photo-heating, corresponding to warm IGM temperatures,  $T \sim 10^4 - 10^{4.5}$  K.

The first case we will consider may be applicable to the case of the recently discovered strong Ne VIII absorber detected by Tripp et al. (2011) in the Cosmic Origins Spectrograph (COS) spectrum of PG1206+459 at  $z \sim 0.927$ . This system is one of the most unique and most puzzling metal absorbers ever observed, containing both high ions like Ne VIII and low ions like Mg II. We explore non-equilibrium photo-ionised models with the AGN on and in the fossil phase. We bolster our argument with evidence for a post-starburst,  $> L^*$  galaxy, possibly within 100 proper kpc, which shows signatures of being an AGN. We use this as a fiducial example to consider variations in AGN strength, lifetime, and duty cycles to show how metal lines can respond to variable ionisation conditions.

We next consider AGN proximity zone fossils at the height of QSO activity at  $z = 2.5$ . The observations of metal-line absorption in transverse QSO proximity zones along the line of sight (e.g. Worseck & Wisotzki 2006; Worseck et al. 2007; Gonçalves et al. 2008) provide our initial motivation, and we extend the exploration to the case where the proximity zones turn into fossil zones after the foreground QSOs turn off. We argue that unique absorption signatures should occur where H I re-equilibrates, but O VI and C IV are still out of equilibrium. We suggest that during the AGN era a large fraction of metal-line systems could reside in proximity zone fossils.

The last example we consider concerns massive, spiral galaxies at  $z = 0.25$  that may recently have harboured active AGN, such as Seyferts, but are currently in the less active or off phase. We demonstrate that increases of at least a dex are possible for circumgalactic (CGM) O VI time-averaged over fossil phases for normal Seyfert luminosities turning on 1 Myr out of every 10 Myr. Our examples show just how sensitive metal lines can be to moderate AGN, even if they are only on for a small fraction of time. As nearly all galaxies are thought to contain supermassive black holes in their centres, fossil proximity zones may be very important for the interpretation of QSO absorption line data.

This paper is organised as follows. We introduce our non-equilibrium code and the methods used in this paper in §2. We apply these methods to the AGN proximity zones and proximity zone fossils for the examples mentioned above in §3, and we summarise in §4. Throughout we use proper distances unless noted otherwise.

## 2 METHOD

We use the non-equilibrium solver introduced in Oppenheimer & Schaye (2013) to follow the time-dependent ionisation states of 11 elements (H, He, C, N, O, Ne, Mg, Si, S, Ca, and Fe). The solver also calculates ion-by-ion cooling and photo-heating to follow the time-dependent non-equilibrium net cooling, defined as cooling minus photo-heating. The code is intended to be integrated in hydrodynamic codes, and includes a treatment to sub-cycle the integration of ionisation and cooling given the input Courant timestep.

In this work, we add the functionality to our method to allow the addition of photo-ionisation and photo-heating from a time variable source, which in this case has the spectral energy distribution (SED) of an AGN. The AGN photo-ionisation rate ( $s^{-1}$ ) for an ionisation state  $i$  of atomic species  $x$  from a radiation source with specific intensity  $f_\nu$  ( $\text{erg s}^{-1} \text{cm}^{-2} \text{Hz}^{-1}$ ) is

$$\Gamma_{x_i, \text{AGN}} = \int_{\nu_{0,x_i}}^{\infty} \frac{f_\nu}{h\nu} \sigma_{x_i}(\nu) d\nu, \quad (1)$$

and the AGN photo-heating rate ( $\text{erg s}^{-1}$ ) is

$$\epsilon_{x_i, \text{AGN}} = \int_{\nu_{0,x_i}}^{\infty} \frac{f_\nu}{h\nu} \sigma_i(\nu) h(\nu - \nu_{0,x_i}) d\nu, \quad (2)$$

where  $\nu$  is frequency,  $\nu_{0,x_i}$  is the ionisation frequency,  $\sigma_{x_i}(\nu)$  is photo-ionisation cross-section, and  $h$  is the Planck constant. Since we track 133 ionisation states of 11 elements, we integrate the above equations for the 122 ionisation states with electrons.

For the EGB, we replace  $f_\nu$  with the ionising background SED averaged over the whole sky,  $4\pi J_\nu$ , in Equations 1 and 2, where  $J_\nu$  has units of  $\text{erg s}^{-1} \text{cm}^{-2} \text{Hz}^{-1} \text{sr}^{-1}$ . As explained in Oppenheimer & Schaye (2013), we calculate  $\Gamma_{\text{EGB}}$  and  $\epsilon_{\text{EGB}}$  at 50 different redshifts between  $z = 0 - 9$  using the Haardt & Madau (2001, hereafter HM01) EGB and the same  $\sigma_{x_i}(\nu)$  used in CLOUDY ver. 10.00 last described in Ferland et al. (1998). We use the HM01 EGB as our fiducial background since this results in good agreement with the observed column density distribution of H I (Davé et al. 2010; Altay et al. 2011) and metal line strengths and ratios (Schaye et al. 2003; Oppenheimer & Davé 2006; Aguirre et al. 2008; Oppenheimer & Davé 2009; Oppenheimer et al. 2012; Rahmati et al. 2012).

The time dependent evolution of the particle number density,  $n$ , for each ionisation state,  $x_i$ , is given by

$$\begin{aligned} \frac{dn_{x_i}}{dt} = & n_{x_{i+1}} \alpha_{x_{i+1}} n_e + n_{x_{i-1}} (\beta_{x_{i-1}} n_e + \Gamma_{x_{i-1}, \text{EGB}} \\ & + \Gamma_{x_{i-1}, \text{AGN}}) - n_{x_i} ((\alpha_{x_i} + \beta_{x_i}) n_e + \Gamma_{x_i, \text{EGB}} + \Gamma_{x_i, \text{AGN}}), \end{aligned} \quad (3)$$

where  $n_e$  is the free electron density ( $\text{cm}^{-3}$ ),  $\alpha_{x_i}$  is the total recombination rate coefficient (radiative plus di-electric,  $\text{cm}^3 \text{s}^{-1}$ ), and  $\beta_{x_i}$  is the collisional ionisation rate coefficient ( $\text{cm}^3 \text{s}^{-1}$ ). The AGN subscript indicates that the coefficients have been calculated using our AGN template spectrum explained below. Charge transfer and Auger ion-

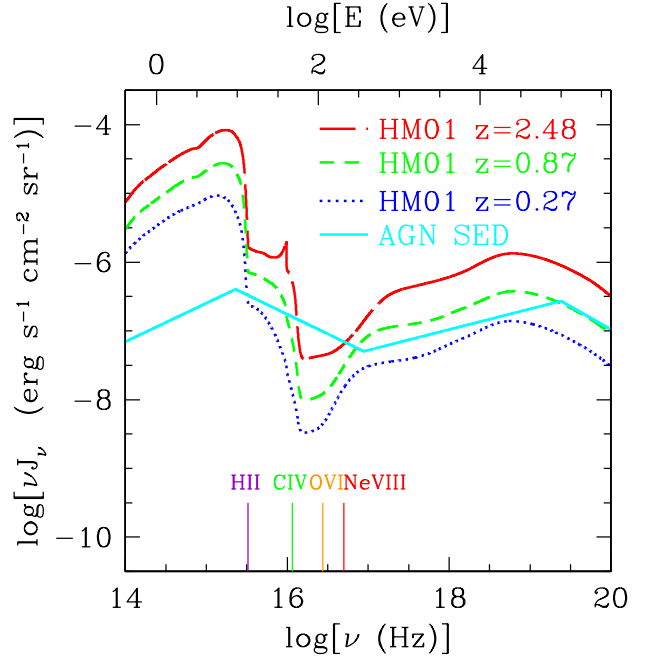


**Figure 1.** The Haardt & Madau (2001) model for the spectrum of the EGB closest to the three redshift regimes ( $z = 2.5, 0.9$  &  $0.25$ ) we consider, along with our AGN template spectrum, normalised to  $J_{\text{LL}} = 10^{-22.0} \text{erg s}^{-1} \text{cm}^{-2} \text{Hz}^{-1} \text{sr}^{-1}$ . The EUV power law of the AGN is  $\nu^{-1.57}$  between  $1300 \text{ \AA}$  and  $354 \text{ eV}$  based on observations by Telfer et al. (2002). The X-ray portion of the spectrum is assumed to follow the CLOUDY AGN template ( $\nu^{-0.7}$  until  $100 \text{ keV}$  and then  $\nu^{-1.67}$  at higher energies). The four coloured vertical lines at the bottom indicate the ionisation potentials needed to reach the corresponding ion listed.

isation are also included in our calculations as explained in Oppenheimer & Schaye (2013), but were omitted from Equation 3 for simplicity.

The net cooling rate per unit volume ( $\Lambda_{\text{net}}$ ,  $\text{erg cm}^{-3} \text{s}^{-1}$ ), is the difference between cooling and photo-heating from the EGB and the AGN,

$$\begin{aligned} \Lambda_{\text{net}, x_i}(T, z, n_{x_i}, n_e) = & \Lambda'_{x_i}(T) n_{x_i} n_e - \epsilon_{x_i, \text{EGB}}(z) n_{x_i} \\ & - \epsilon_{x_i, \text{AGN}}(z) n_{x_i}. \end{aligned} \quad (4)$$

The units of the cooling efficiency per ion,  $\Lambda'_{x_i}$  are  $\text{erg cm}^3 \text{s}^{-1}$ , where we divided the cooling rate per volume ( $\text{erg cm}^{-3} \text{s}^{-1}$ ) for ion  $x_i$  by  $n_{x_i} n_e$  to achieve density independence of collisional cooling, which allows us to tabulate these rates as a function of temperature only.

Figure 1 compares our AGN template spectrum,  $f_\nu$  to the HM01 EGB,  $J_\nu(z)$  at the three different redshifts ( $z = 2.48, 0.87$ , and  $0.27$ ) nearest the three redshifts we consider in this paper ( $z = 2.5, 0.9$ , and  $0.25$ ). The HM01 EGB strength at the Lyman limit at these three redshifts is from high to low- $z$   $\log[J_{\text{LL}} (\text{erg s}^{-1} \text{cm}^{-2} \text{Hz}^{-1} \text{sr}^{-1})] = -21.30, -21.64$ , and  $-22.16$ .

In cyan is the AGN SED normalised to  $f_{\text{LL}} = 10^{-20.9} \text{erg s}^{-1} \text{cm}^{-2} \text{Hz}^{-1}$ . Since this is a point source, we can convert its flux into  $J_{\text{LL}}$  equivalent units by dividing by  $4\pi$  steradians to get  $J_{\text{LL}, \text{equ}} =$

$10^{-22.0} \text{erg s}^{-1} \text{cm}^{-2} \text{Hz}^{-1} \text{sr}^{-1}$ , which has the same units as the EGB. Hence,  $J_{\text{LL, equ}}$  is the intensity the EGB would have if it were equally bright as the AGN at the Lyman limit. The spectrum has an EUV power law with slope  $\nu^{-1.57}$  between 1300 Å and 354 eV based on observations by Telfer et al. (2002). At higher energies, the spectrum follows  $\nu^{-0.7}$  until 100 keV and then  $\nu^{-1.67}$  at higher energies, which follows the template CLOUDY AGN spectrum. The most important slope for our consideration is the EUV (i.e. 10-354 eV) slope, because these energies correspond to the ionisation potentials of the metal species we consider and which are marked in Figure 1. However, the X-ray portion of the spectrum is also important for two reasons: i) photo-heating rates of species like O VII and O VIII depend on the shape of the X-ray spectrum, and ii) we convert to observed luminosities of AGN based on their 0.5-2.0 keV luminosities ( $L_{0.5-2.0}$ ).

To convert these units to AGN luminosities, the above flux ( $f_{\text{LL}} = 10^{-20.9} \text{erg s}^{-1} \text{cm}^{-2} \text{Hz}^{-1}$ ) corresponds to  $L_{0.5-2.0} = 10^{42.1} \text{erg s}^{-1}$  AGN at 100 proper kpc, which is the luminosity one may expect from a local Seyfert. The Seyfert would outshine the  $z = 0.25$  HM01 EGB at 912 Å by 45% at 100 kpc, but because of the harder AGN spectrum at the O VI photo-ionisation edge, 114 eV, the AGN would outshine the HM01 spectrum by a factor of 23×, assuming no absorption of the AGN spectrum. In general, for our template AGN spectrum the conversion from AGN soft X-ray luminosity to equivalent EGB intensity units is

$$J_{\text{LL, equ}} = \frac{f_{\text{LL}}}{4\pi} = 10^{-22} \left( \frac{r_{\text{AGN}}}{100 \text{ kpc}} \right)^{-2} \left( \frac{L_{0.5-2.0}}{10^{42.1} \text{erg s}^{-1}} \right) \text{erg s}^{-1} \text{cm}^{-2} \text{Hz}^{-1} \text{sr}^{-1}, \quad (5)$$

where  $r_{\text{AGN}}$  is the proper distance from the AGN.

### 3 APPLICATIONS OF AGN PROXIMITY ZONE FOSSILS

We consider three situations spanning a wide range of redshifts, from  $z = 2.5$  to 0.25, that are applicable to recent observations. In all cases we assume the gas is being irradiated by the HM01 EGB for the given redshift, and that it initially has the equilibrium temperature for which photo-heating balances cooling. This temperature corresponds to  $T \sim 10^{3.85-4.68}$  K assuming solar abundances for the densities we consider,  $n_{\text{H}} = 10^{-5.0} - 10^{-3.0} \text{cm}^{-3}$ . The main reasoning behind our parameter choices is that simulations indicate that a significant fraction of diffuse metals reside along a locus in density-temperature phase space where photo-heating balances cooling (e.g. Oppenheimer & Davé 2006; Wiersma et al. 2010, 2011), and that many commonly observed metal-line species arise from gas at these densities and temperatures (e.g. Oppenheimer et al. 2012). Although solar abundances are used, we will argue that our theoretical metal columns scale nearly linearly with metallicity.

In §3.1 we discuss our first application: an AGN turning on at  $z = 0.9$ , which is motivated by observations of the very strong Ne VIII system observed by Tripp et al. (2011) toward PG1206+459, which appears to reside near a galaxy showing signs of AGN activity. We pay particular attention to this

example, because of the large number of metal-line species observed in this system and also because Ne VIII is one of the species most affected by AGN ionisation. We vary several parameters including metallicity, density, AGN strength, and AGN lifetime. In §3.2, we consider the effects on C IV, N V, and O VI columns at  $z = 2.5$ , both when a quasar is on and after it turns off. We estimate the fraction of the volume of the IGM altered by fossil zones, and argue that a large fraction of observed metal lines may be affected. Lastly, in §3.3, we explore short duty cycles of  $z = 0.25$  AGN that significantly enhance O VI columns, even while the AGN is off. This case could be applicable to normal looking spirals that were recently Seyferts, where residual non-equilibrium effects of AGN ionisation enhance metal columns.

The general behaviour that we find can be summarised as follows. The enhanced photo-ionisation from the AGN rapidly raises the ionisation states of metals, thus allowing high-ionisation species to exist at higher densities than they would in equilibrium with the normal EGB. After the AGN turns off, the long recombination times of metals, along with the multi-ionisation state nature of metals and their significant ionisation fractions (i.e.  $f_{x_i} \gtrsim 0.1$  for multiple  $i$ ), mean that metal columns often only return to equilibrium on a timescale that is longer than the AGN-on phase. Thus, a whole new range of ionisation models that have not been considered are allowed.

#### 3.1 AGN fossil zones at $z = 0.9$

In our fiducial example, we consider the effects of an enhanced ionisation in the proximity zone around an AGN that is on for 20 Myr at  $z = 0.9$ . This case is directly applicable to observations by COS at a redshift where a large array of both low- and high-ionisation species can be observed. This example is motivated by the extremely strong Ne VIII ( $N_{\text{Ne VIII}} \sim 10^{15} \text{cm}^{-2}$ ) absorber observed by Tripp et al. (2011) at  $z = 0.927$  along the PG1206+459 sight line with well-aligned lower ionisation species. A foreground galaxy, labelled 177<sub>9</sub> by that work, found at the same redshift at an impact parameter of 68 kpc, shows signs of being a post-starburst galaxy with a  $B$ -band absolute magnitude of  $-22$  and even AGN signatures from [Ne V] emission that likely cannot be explained by star formation alone.

Figure 2 shows the time evolution of gas enriched to solar metallicity with  $n_{\text{H}} = 10^{-4} \text{cm}^{-3}$ , which corresponds to an overdensity of 77 at  $z = 0.9$  (assuming  $\Omega_b = 0.046$  and a hydrogen mass fraction of 0.75). This choice represents a typical density of metal-enriched CGM gas. The gas is assumed to lie at its equilibrium temperature,  $T = 10^{4.23}$  K, when we mimic the instantaneous turn-on of the AGN by adding our template AGN spectrum to the HM01 EGB at that redshift. We assume an AGN flux of  $f_{\text{LL}} = 10^{-18.9} \text{erg s}^{-1} \text{cm}^{-2} \text{Hz}^{-1}$ , which has the H I ionisation equivalence of a uniform EGB with  $J_{\text{LL, equ}} = 10^{-20.0} \text{erg s}^{-1} \text{cm}^{-2} \text{Hz}^{-1} \text{sr}^{-1}$  integrated over  $4\pi$  steradians; this corresponds to 44× the EGB value and a total ionisation parameter  $\log[U] = 0.3$ , where  $U$  is the ratio of hydrogen ionising photon density over  $n_{\text{H}}$ . Using our template spectrum and integrating over the soft X-ray band (0.5-2.0 keV), we calculate that this is the flux at 100 kpc from a  $L_{0.5-2.0} = 10^{44.11} \text{erg s}^{-1}$  AGN, which appears to be a rea-

reasonable assumption given the observed impact parameter of 68 kpc for galaxy 1779.

In the top panel we show the column densities of several observationally accessible ions by assuming an absorber length of 52 kpc, which is the predicted size of an H I absorber at this density and temperature according to Equation 3 of Schaye (2001). All column densities scale linearly with the assumed absorber size. As the AGN turns on at  $t = 0$ , the H I column density and ionisation fraction drop nearly instantaneously by a factor of 44 as  $\tau_{\text{ion,H I}}$  is only 1100 yr for this field.<sup>1</sup> The ionisation timescales for the metal species, shown in the middle panel of Figure 2 during the AGN-on phase (thick dotted lines) are longer, 0.1 – 5 Myr, but still less than the assumed AGN lifetime of 20 Myr. During the AGN-on phase, the species O VI, Ne VIII, and Mg X first rise to a peak and then fall as they are first ionised from lower ions to these states and then to higher ions, owing to the large increase in the radiation field. On the other hand, C IV, which initially comprises 27% of carbon, decreases dramatically as carbon is ionised all the way to C VII in under 10 Myr.

The column densities in the AGN-on phase are applicable to proximate quasar absorption line (QAL) systems observed near the background source quasar, or to intervening QAL systems where the local ionising field is significantly enhanced by foreground AGN near the sight line to the background source quasar. Absorption systems with  $\log[U] = 0.3$  will have Ne VIII column densities that are 80 – 300 $\times$  stronger than for the HM01 field where  $\log[U] = -1.3$  at  $n_{\text{H}} = 10^{-4} \text{cm}^{-3}$ , while  $N_{\text{H I}}$  will be reduced by a factor of 50, and  $N_{\text{C IV}}$  will be reduced even more.  $N_{\text{O VI}}$  can either increase or decrease depending on the AGN lifetime. Mg X is the most enhanced photo-ionised species shown, increasing more than  $10^4 \times$  in strength to  $10^{14.3} \text{cm}^{-3}$ .

The temperature increases by 29% to  $T = 10^{4.33}$  K due to photo-heating by the strongly increased ionising field (bottom panel). The temperature increase results primarily from the ejection of highly energetic electrons by X-ray photons leading to high-ionisation metal species (e.g. C V, O VII, and O VIII). For this solar-enriched case, metal photo-heating dominates over that from He II, which has a lower ionisation potential than metal ions. The photo-heating of H I does not contribute to the temperature increase, because in ionisation equilibrium the increase in the radiation field is exactly compensated by the corresponding decrease in the neutral fraction, and the latter is too small to result in significant non-equilibrium heating.

The AGN proximity zone fossil phase begins after the AGN turns off and the ionisation field switches back to the uniform HM01 EGB. The solid thin lines in the middle panel indicate the recombination timescales of the various species. Although  $\tau_{\text{rec,H I}} \sim 10^9$  yr,  $N_{\text{H I}}$  reaches equilibrium in a much smaller timescale,  $\sim 10^{4.7}$  yr, because the equilibrium neutral fraction it has to return to is only  $f_{\text{H I}} = 10^{-4.3}$ . In contrast, fossil ionised bubbles around dead quasars can persist for  $\sim \tau_{\text{rec,H I}}$  during reionisation since the equilib-

rium state is neutral (Furlanetto et al. 2008); however, we are considering only cases where an EGB ionises the IGM to a high level.  $N_{\text{H I}}$  remains slightly smaller than before  $t = 0$ , because photo-heating increased the temperature of the gas, thereby reducing the recombination rate. The cooling timescale of  $\sim 1$  Gyr means that the gas will take of order this time to approach the original equilibrium temperature and H I fraction.

Even though the Helium-like metal ion recombination timescales (solid lines in the middle panel of Figure 2) are  $\sim 20 - 180 \times$  shorter than for H II, their recombination lags are 100 – 900 $\times$  longer than for H I, because the equilibrium ion fractions are a significant fraction of unity. A case in point is the timescale of  $\sim 50$  Myr that it takes C IV columns to approach their previous equilibrium values. A series of recombination timescales of species between C VII and C V determine the total time it takes C IV to return to equilibrium, since carbon is primarily in C VII when the AGN turns off. However, the longest is  $\tau_{\text{rec,C V}} \sim 40$  Myr, shown as the green solid line in the middle panel.

O VI is significantly enhanced during  $\sim 70$  Myr after the AGN turns off, even though its column density is decreased during the AGN-on phase. O VI achieves at least twice as large columns between 33-74 Myr, as oxygen recombines from a majority of O VIII at  $t = 20$  Myr to O IV at  $t = 95$  Myr.  $\tau_{\text{rec,O VII}} = 20$  Myr is the bottleneck slowing the recombination sequence (orange solid line in the middle panel).

The most dramatic residual observable change is for Ne VIII, for which columns increase 100 fold for the first 15 Myr of the fossil phase and remain at least  $10 \times$  stronger for 50 Myr. Despite the main recombination bottleneck being  $\tau_{\text{rec,Ne IX}} = 10$  Myr, or about half as long as  $\tau_{\text{rec,O VI}}$ , Ne VIII takes several recombination times to approach its very low equilibrium value. Thus  $N_{\text{Ne VIII}} \sim 10^{14} \text{cm}^{-2}$ , which has been observed and attributed to collisionally ionised gas at  $T \sim 10^6$  K (Savage et al. 2005; Narayanan et al. 2009, 2011), could have an alternative colder origin if nearby galaxies currently or recently harboured an AGN. In passing, we note the recent work of Muzahid et al. (2013), who find extremely strong high ionisation lines (e.g. Ne VIII, Mg X) in associated QSO absorbers, which are possibly photo-ionised by the AGN; however, we note that those absorbers are probably located much nearer to the supermassive black hole than the extended proximity zones that are the focus of the present study.

### 3.1.1 Parameter variations

We have considered the very specific example of an AGN proximity zone fossil applicable to enriched gas at CGM densities (i.e. overdensities  $\gtrsim 50$ ). While our choices appear reasonable, we wish to broaden the range of physical parameters and situations by varying the metallicity, density, AGN strength, and AGN lifetime. We will relate these variations to situations that may occur in the real Universe and will argue that fossil zones could significantly change the interpretation of metal QAL observations. We will continue to assume that the metals are cool ( $T \sim 10^4 - 10^{4.5}$  K), residing at the equilibrium temperature where photo-heating balances radiative cooling.

**Metallicity:** Choosing solar metallicity for an absorption

<sup>1</sup> Note that the ionisation timescale is shorter than the light travel times from the AGN to the absorber, which we do not consider.

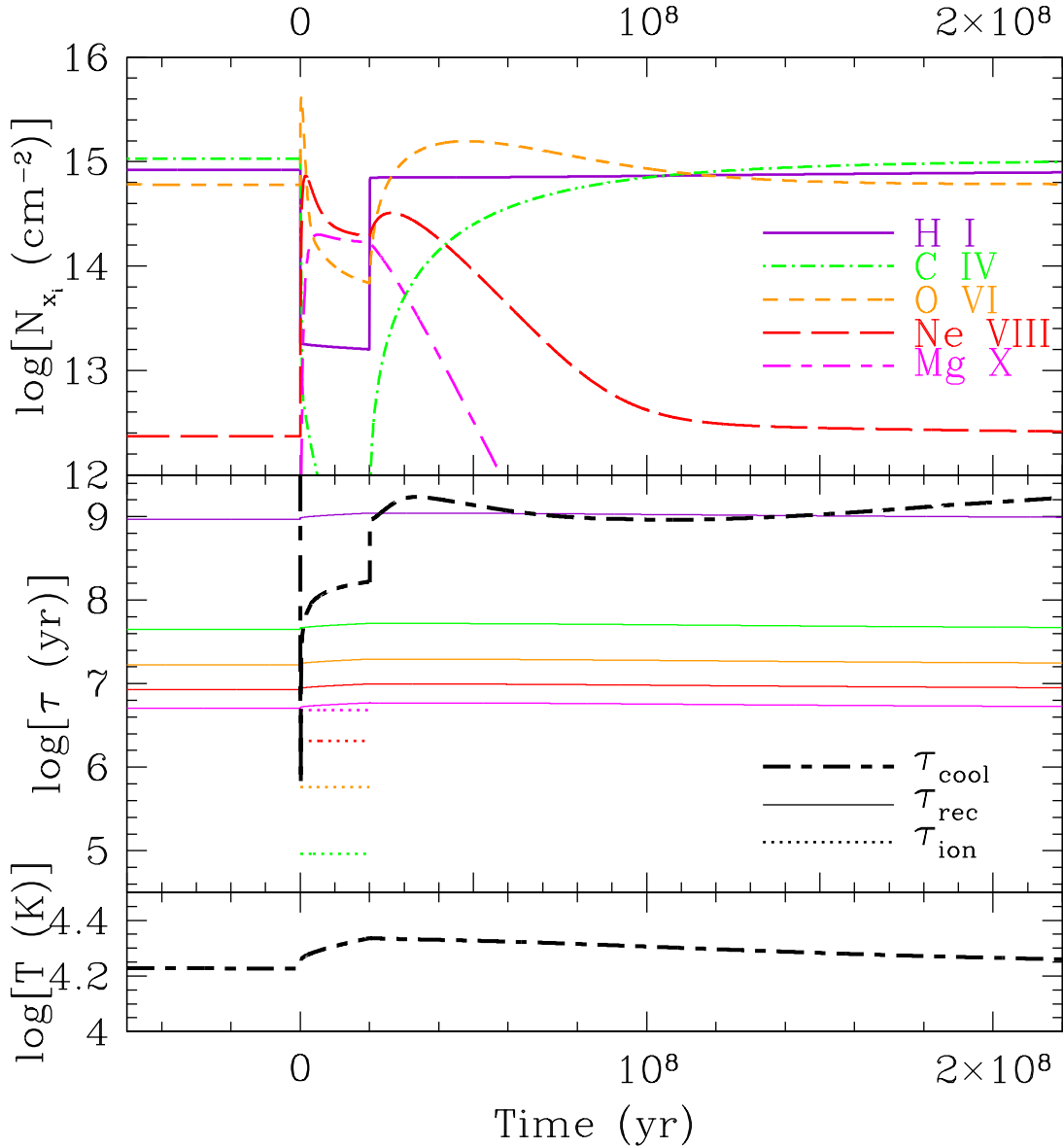


**Figure 2.** The evolution of a  $n_{\text{H}} = 10^{-4} \text{ cm}^{-3}$ , 52 kpc, solar abundance absorber irradiated by the  $z = 0.9$  HM01 EGB when an AGN with intensity  $J_{\text{LL, equ}} = 10^{-20} \text{ erg s}^{-1} \text{ cm}^{-2} \text{ Hz}^{-1} \text{ sr}^{-1}$  ( $L_{0.5-2.0} = 10^{44.1} \text{ erg s}^{-1}$  at 100 kpc distance) turns on at  $t = 0$  for 20 Myr. After 20 Myr the AGN turns off but the long recombination times of Helium-like metal ions (C v, O vii, Ne ix, & Mg xi; between 5-50 Myr; middle panel, solid thin lines) cause these observable Lithium-like ions to take longer than the AGN-on time to reach their equilibrium levels. Ionisation timescales of the Lithium-like ions (middle panel, thick dotted lines shown only when the AGN is on) are shorter than 20 Myr when the AGN is on. Photo-heating, primarily of metals, results in a slightly increased temperature of the gas that cools on a timescale of 1 Gyr (middle panel, thick black dashed lines). Unlike metals and despite a 1 Gyr recombination timescale, hydrogen rapidly recombines to equilibrium when the AGN turns off, owing to its very small equilibrium neutral fraction. The columns scale linearly with the assumed absorber length and metallicity.

system is not unprecedented as detailed analysis of observed systems often yield solutions with solar or super-solar metallicities (Péroux et al. 2006; Prochaska et al. 2006; Schaye et al. 2007; Tripp et al. 2011; Tumlinson et al. 2011). However, many of these systems are attributed to lower density gas, which may on average be enriched to lower levels if metallicity increases with density as observations and simulations indicate (e.g. Schaye et al. 2003; Oppenheimer & Davé 2006, 2009; Wiersma et al. 2010, 2011). Lowering the metallicity does not alter the recombination timescales or behaviour significantly. The equilibrium temperature in the HM01 ionisation field increases from  $T = 10^{4.23}$  K for  $Z = Z_{\odot}$  to  $10^{4.49}$  K for  $0.1 Z_{\odot}$ , owing to reduced metal-line cooling, and this results in only a 0.2 dex reduction of  $N_{\text{HI}}$ . Hence, metal-line strengths as a function of time can, to first order, be scaled with  $Z$ . However, if intergalactic metals are poorly mixed on small scales as some observations and simulations indicate (Simcoe et al. 2006; Schaye et al. 2007; Oppenheimer & Davé 2009; Tepper-Garcia et al. 2011), then high metallicities may even be appropriate at low densities.

**Density:** Changing the density alters the non-equilibrium behaviour because the recombination timescale as  $n_{\text{H}}^{-1}$ . The ionisation parameter also changes when assuming a constant radiation field, meaning that in equilibrium atomic species are photo-ionised to higher ion states at lower densities. We explore here four densities:  $n_{\text{H}} = 10^{-5.0}$ ,  $10^{-4.5}$ ,  $10^{-4.0}$ , and  $10^{-3.5} \text{ cm}^{-3}$  corresponding to  $z = 0.90$  overdensities  $\rho/\langle\rho\rangle = 7.7$ , 24, 77, and 243 respectively. We assume an absorber length set by the Schaye (2001) relation ( $l = 0.52n_{\text{H}}^{-0.5} \sqrt{T/10^4}$  kpc), which equals the Jeans scale in a gas of uniform density and temperature. We set  $T = 10^4$  K in the previous equation for simplicity, even though temperatures are usually slightly higher. This size scale, which ranges from 164 to 29 kpc for our densities, has been shown to reproduce the observed sizes of the Ly $\alpha$  absorbers (e.g. Schaye 2001; Prochaska et al. 2004; Lehner et al. 2007) and agrees very well with predictions from hydrodynamic simulations (Davé et al. 2010; Tepper-García et al. 2012; Rahmati et al. 2012).

Figure 3, top panel, shows that the  $N_{\text{HI}}$  of the absorbers initially range from  $10^{13.2} \rightarrow 10^{15.8} \text{ cm}^{-2}$  with increasing density, which correspond to observed Ly $\alpha$  absorbers that typically exhibit detectable metal-line absorption (Danforth & Shull 2008; Thom & Chen 2008b; Tripp et al. 2008; Tilton et al. 2012). As the AGN radiation field turns on and off,  $N_{\text{HI}}$  reduces and increases by a factor 50 on timescales that are too short to appear in the figure. A slight deviation occurs for higher densities where photo-heating raises the temperature during the AGN more, owing to the greater number of bound electrons available to ionise from metals. Although lower densities have a smaller photo-heating temperature increases (bottom panel), the longer cooling times of several Gyr mean that a 20 Myr AGN phase has longer lasting effects on the temperature of the IGM.

The third panel in Figure 3 shows  $N_{\text{OVI}}$  for the four densities. The overdensity range we explore covers nearly the same range that simulations predict observed O VI absorbers to arise from at  $z < 0.5$  (e.g. Oppenheimer & Davé 2009; Tepper-Garcia et al. 2011; Cen & Chisari 2011; Smith et al. 2011; Oppenheimer et al. 2012). When the AGN turns on,

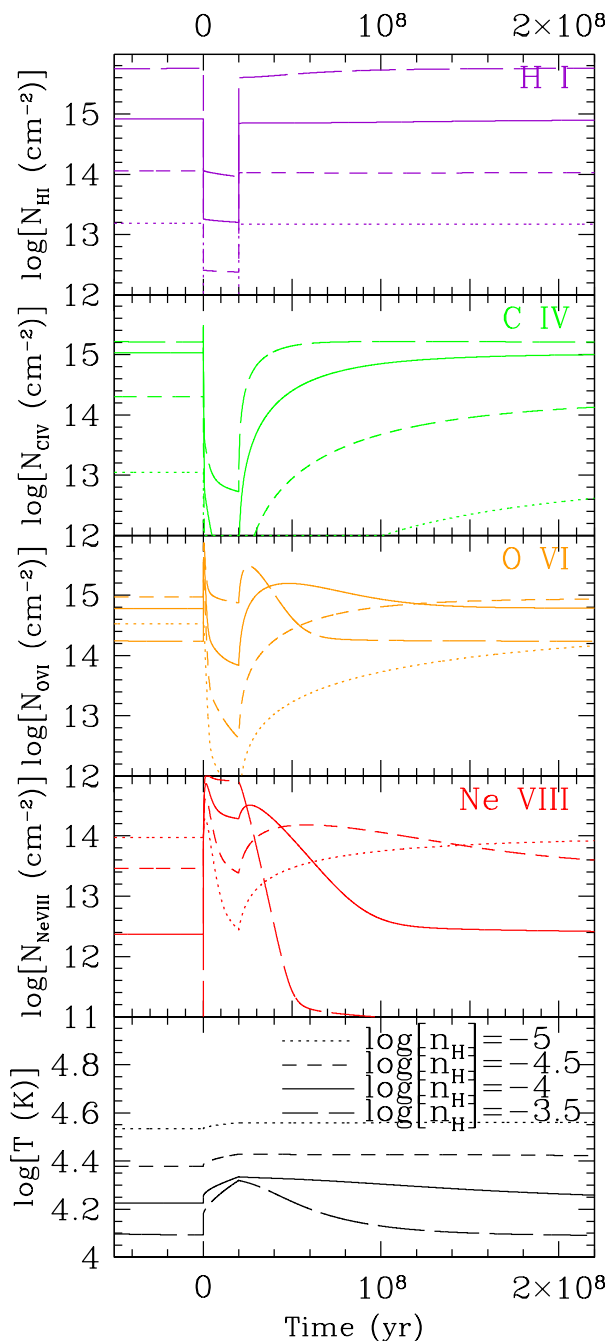


**Figure 3.** The density dependence of the non-equilibrium proximity effect at  $z = 0.9$  using an AGN with  $J_{\text{LL, equ}} = 10^{-20.0} \text{ erg s}^{-1} \text{ cm}^{-2} \text{ Hz}^{-1} \text{ sr}^{-1}$  turning on at  $t = 0$  for 20 Myr. The assumed absorber lengths decrease from 164 to 29 kpc as density increases from  $n_{\text{H}} = 10^{-5.0}$  to  $10^{-3.5} \text{ cm}^{-3}$ .  $N_{\text{HI}}$ ,  $N_{\text{CIV}}$ ,  $N_{\text{OVI}}$ ,  $N_{\text{NeVIII}}$ , and temperature evolution are shown from top to bottom. Ionisation timescales remain unaltered between the four cases, but recombination timescale as  $n_{\text{H}}^{-1}$  meaning that the fossil effect will last longer at lower density. Metallicity is assumed to be solar in all cases, but metal columns scale with metallicity with the minor exception that photo-heating will be lower at lower metallicity and temperatures will not vary as much.

the ionisation timescales are independent of  $n_{\text{H}}$ , but the new ionisation equilibrium does depend on  $n_{\text{H}}$ . For  $n_{\text{H}} \leq 10^{-4} \text{cm}^{-3}$  oxygen is ionised from O VI to higher states reducing these columns, while for  $n_{\text{H}} \geq 10^{-3.5} \text{cm}^{-3}$  lower ionisation oxygen is ionised to O VI increasing the columns. When the AGN turns off, lower densities take longer to return to ionisation equilibrium because recombination timescale inversely with  $n_{\text{H}}$ . Thus, while the lowest density will have deficient O VI relative to the equilibrium case for  $> 100$  Myr, the highest overdensity will have enhanced O VI for a shorter timescale, similar to the AGN lifetime of 20 Myr in this case.

In contrast to O VI,  $N_{\text{CIV}}$  is reduced by the AGN for all densities while  $N_{\text{NeVIII}}$  shows an increase for  $n_{\text{H}} \geq 10^{-4.5} \text{cm}^{-3}$  (2nd & 4th panels of Figure 3 respectively). The C IV ionisation fraction peaks at  $n_{\text{H}} = 10^{-3.9} \text{cm}^{-3}$  when photo-ionised by the  $z = 0.9$  HM01 field at  $T \sim 10^4$  K. Turning on the AGN shifts this peak to  $n_{\text{H}} = 10^{-1.3} \text{cm}^{-3}$ . Hence, C IV will be reduced by the AGN, and the lowest densities will take the longest to recombine from higher ions in the fossil zone. Conversely, the ionisation fraction of Ne VIII peaks at  $n_{\text{H}} = 10^{-5.5} \text{cm}^{-3}$  at  $T \sim 10^4$  K, which shifts to  $10^{-3.3} \text{cm}^{-3}$  with the AGN. Hence, gas with  $n_{\text{H}} = 10^{-3.5} \text{cm}^{-3}$  can have  $N_{\text{NeVIII}}$  columns as high as  $10^{15} \text{cm}^{-2}$  during the AGN phase, 12,000 $\times$  larger than for the HM01 field in equilibrium. The recombination times of a few Myr means that this strong Ne VIII will be shorter lived in the fossil zone.

**AGN radiation field increase:** In Figure 4, we consider field increases,  $J_{\text{LL, equ}}$  of factors 4.4 and 440 to simulate the AGN proximity effect at 3.16 and 0.32 $\times$  the fiducial radius (i.e. 316 and 32 kpc) respectively for the same strength AGN. Or alternatively, an AGN 0.1 and 10 $\times$  as strong at 100 kpc. We again use our fiducial density  $n_{\text{H}} = 10^{-4.0} \text{cm}^{-3}$ . The ionisation timescales decrease in proportion to the field increase, and stronger radiation fields cause metals to become more ionised in a shorter amount of time. However, post-AGN metal-line strengths show qualitatively similar evolution, because the recombination timescales are the same. There is a greater delay for stronger fields, reflecting the additional recombination time from even higher ionisation states (e.g.  $\tau_{\text{rec, CIV}}$ ,  $\tau_{\text{rec, OVIII}}$ ). Even for  $J_{\text{LL, equ}} = 10^{-21} \text{erg s}^{-1} \text{cm}^{-2} \text{Hz}^{-1} \text{sr}^{-1}$ , which corresponds only to a factor 4.4 $\times$  increase relative to the EGB, significant enhancements are seen, especially in Ne VIII. The field increase is insufficient to ionise to Ne IX, but post-AGN Ne VIII columns are enhanced 100 $\times$  and decline slowly according to  $\tau_{\text{rec, NeVIII}}$ . Considering that the 10 $\times$  smaller field increase applies to  $10^{3/2} \sim 32\times$  more volume, the weaker field case could be most relevant to intervening QAL, which provide a volume-weighted sampling of the IGM.

**AGN lifetime:** Thus far we have assumed a single  $\tau_{\text{AGN}} = 20$  Myr lifetime, but AGN lifetimes are predicted to be as short as  $10^6$  yr. Figure 5 shows what happens if an AGN is on for shorter periods at multiple times. We choose to show an AGN that is on 5 out of every 50 Myr yielding a duty cycle,  $d = 10\%$ , and an AGN that is on 1 out of every 25 Myr, yielding  $d = 4\%$ . For metals, the effect of a shorter lifetime is similar as that of a weaker AGN: they are not as highly ionised by the AGN, but the post-AGN recombination times are the same. A shorter  $\tau_{\text{AGN}}$  results in metals not reaching as highly ionised states. Post-AGN, the metals are less likely

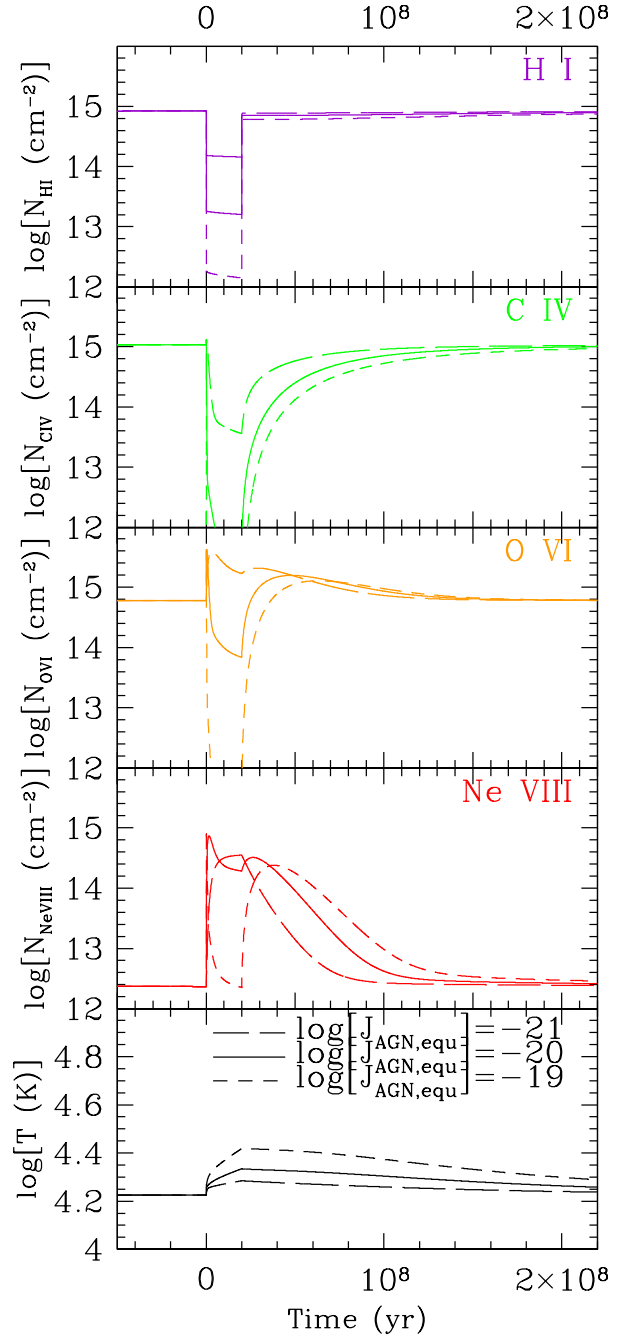


**Figure 4.** The dependence of the non-equilibrium proximity effect on AGN strength at  $z = 0.9$  with  $n_{\text{H}} = 10^{-4} \text{cm}^{-3}$  and  $l = 52$  kpc for an AGN turning on at  $t = 0$  for 20 Myr. The AGN flux enhancement relative to the HM01 EGB ranges from a factor of 4.4 (long dashed lines) to 440 (short dashed lines). The stronger the AGN flux, the higher the ionisation state that the metals reach, and the more delayed the recombination to equilibrium becomes owing to the need to recombine through more ionisation states with significant recombination times. Although the metallicity is assumed to be solar, the metal columns scale with metallicity, except for the minor effect of photo-heating being less efficient at lower metallicity.



to have to recombine through these upper states reducing the number of recombination times to return to equilibrium. Nevertheless, the most significant bottleneck is the longest metal  $\tau_{\text{rec}}$  from the Helium-like state (C V, O VII, Ne IX) to the Lithium-like ions we plot. Hence metal-line evolution is often similar in these three cases although shifted in time depending on the strength and of course the frequency of AGN-on phases.

Even short AGN lifetimes can efficiently enhance metal columns if the duty cycle is similar to or smaller than the recombination times. A case in point is Ne VIII for  $\tau_{\text{AGN}} = 1$  Myr in the 4th panel, whose column density is enhanced by  $60\times$  averaged over 0-200 Myr, despite the AGN being on only 4% of the time. For  $\tau_{\text{AGN}} = 1$  Myr, O VI is enhanced by a factor of three and remains relatively constant, owing to a coincidence:  $\tau_{\text{ion,OVI}} \sim 1$  Myr is similar to  $\tau_{\text{AGN}}$ , and  $\tau_{\text{rec,OVII}} \sim 20$  Myr is similar to the duty cycle timescale of 25 Myr. The implications for small duty cycles with resonances that amplify the fossil effect will be explored further in §3.3. Finally, the bottom panel shows how duty cycles can pump temperatures up, owing to the combination of short photo-heating timescales and long cooling timescales if the gas has solar metallicity.

**Extra-galactic background and AGN EUV power laws:** We have chosen an AGN spectrum with an EUV power law of  $\nu^{-1.57}$  based on Telfer et al. (2002). The local AGN ionises diffuse gas that is additionally ionised by the HM01 spectrum, which itself assumes a QSO EUV input of  $\nu^{-1.80}$ . If we used either the Haardt & Madau (1996) or Haardt & Madau (2012) EGBs that use hard QSO input spectra of  $\nu^{-1.50}$  and  $\nu^{-1.57}$  respectively, then the increase in the radiation field at the ionisation potentials of high ions like O VI, Ne VIII, and Mg X would be more muted. The general behaviour explored above would still be applicable, but the ionisation equilibrium with the EGB would be more highly ionised.

In the real Universe, there exists an extremely large range of observed AGN EUV power laws. Telfer et al. (2002) and Shull et al. (2012) together find a range of  $\nu^{-3}$  to  $\nu^0$  encompassing most of their measured AGN, and even an outlier with  $\nu^{0.56}$ , which is the well-known quasar HE2347-4342 at  $z = 2.9$  that has been used as a probe of He II reionisation (Shull et al. 2010). Hence, the fossil effect may be even greater for harder AGN, which are more capable of ionising high ions, while softer AGN will have much less of an effect. Interestingly, Scott et al. (2004) provide a sample showing an anti-correlation between EUV hardness and AGN luminosity. Their composite spectrum has a harder EUV slope,  $\nu^{-0.56}$ , than Telfer et al. (2002) and Shull et al. (2012), which suggests greater fossil effects. In fact, they find that their lowest luminosity AGN have EUV slopes exceeding 0.0 in the low-redshift Universe, which makes our exploration of weak AGN in §3.3 possibly even more relevant.

### 3.1.2 Direct modelling of the $z = 0.927$ PG1206+459 Ne VIII absorber

We show more detailed results for our fiducial model in Figure 6, where we plot the evolution of the column densities of some metal-line species observed by Tripp et al. (2011) and H I against Ne VIII for the example shown in Figure 2. We

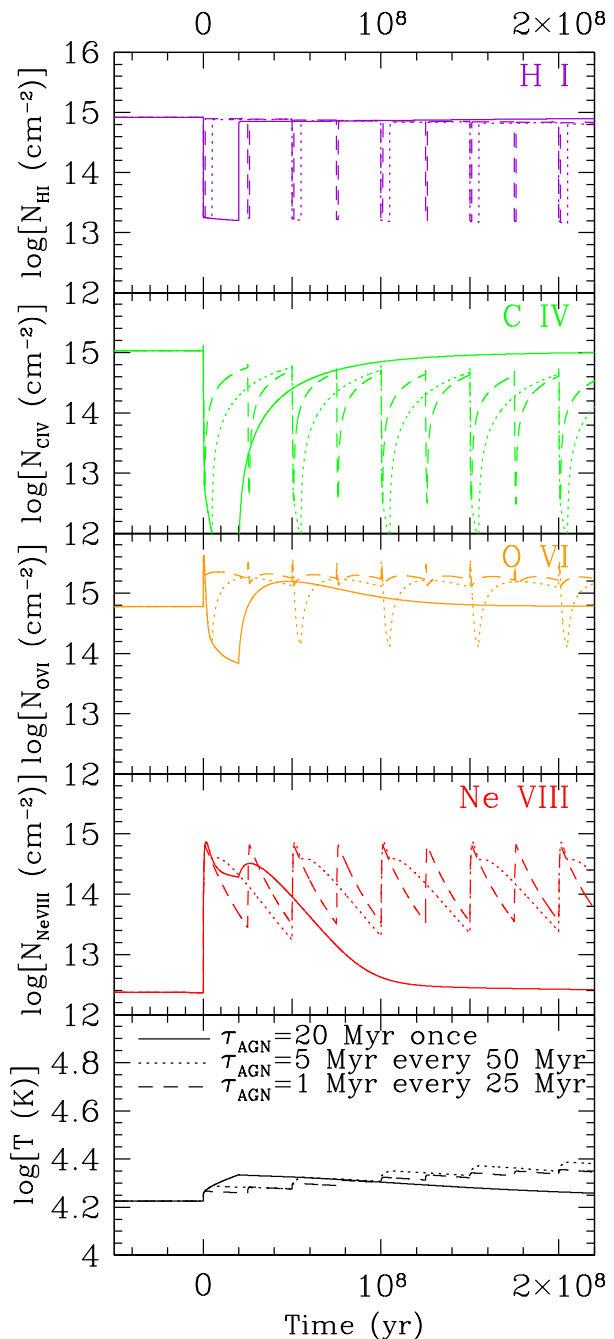


**Figure 5.** Different AGN lifetime and duty cycle variations of the non-equilibrium proximity effect at  $z = 0.9$  with  $n_{\text{H}} = 10^{-4} \text{ cm}^{-3}$  and  $l = 52$  kpc for an AGN flux of  $J_{\text{LL, equ}} = 10^{-20} \text{ erg s}^{-1} \text{ cm}^{-2} \text{ Hz}^{-1} \text{ sr}^{-1}$ . We compare our fiducial case of a single AGN-on phase of 20 Myr with an AGN-on phase of 5 Myr every 50 Myr and 1 Myr every 25 Myr. The first AGN on phase always starts at  $t = 0$ . Significant non-equilibrium behaviour occurs in all cases significantly altering the time-averaged column densities during the AGN-off phase. Photo-heating in bursts can boost average gas temperatures as well. Although the metallicity is assumed to be solar, the metal columns scale with metallicity, except for the minor effect of photo-heating being less efficient at lower metallicity.

plot the coloured diamonds every  $10^5$  yr starting at  $t = 0$  when the AGN turns on (large magenta diamond). The upper left panel shows the evolution of N V and Ne VIII. The ionisation timescales imply that these ions take several Myr to approach the AGN-on equilibrium. At 20 Myr the AGN turns off (indicated as a white line in the colour bar in the lower left panel), and the evolution back to the normal HM01 EGB equilibrium is much slower, taking over 100 Myr.

The open squares show the Tripp et al. (2011) component absorbers, indicating lower limits for saturated absorbers as triangles in the case of O IV, and upper limits as upside-down triangles for non-detections of Mg X. We combine their +65 and +108 km s<sup>-1</sup> components into one motivated by the blended Ne VIII detection. While photo-ionised Ne VIII is far too weak without an AGN, the AGN ionisation achieves the observed Ne VIII columns within 0.5 Myr. A possible scenario for this absorber is an AGN that has been off for  $\sim 30$  Myr, as most Ne VIII, N V, S V, Mg X, and O IV components are then within the allowed ranges. However, Mg II is underestimated by up to a factor  $10^4$ , and H I is too low even after the AGN has turned off. This illustrates the need for a multi-phase model with a component for the lower ionisation species that is shielded from the AGN or which arises in much denser gas.

Another possible scenario in Figure 6 is the AGN just turning on for a few  $\times 10^5$  yr producing reasonable columns for higher ionisation species (N V, S V, Ne VIII, Mg X), but requiring a second phase for lower ionisation species (H I, Mg II, O IV). After all, galaxy 177<sub>9</sub> does show active AGN signatures. This scenario is, however, a priori less likely since  $10^5 \ll 10^7$  yr.

Figure 6 shows merely one possible time-dependent history for an AGN ionising cool, metal-enriched gas. A weaker AGN strength provides nearly as good a fit. A higher density,  $n_{\text{H}} = 10^{-3.5} \text{ cm}^{-3}$ , model where the AGN turned off 10 Myr before fits the columns just as well, but produces  $100\times$  stronger Mg II, which is however still  $\sim 100\times$  too low. Our point is that models with time-dependent AGN that have either turned off in the past, recently turned on, or fluctuate are worth considering, especially for the extreme case of the PG1206+459 absorber with evidence of a post-starburst AGN within 100 kpc of the sight line. The difficulty is that a wide range of models are possible, most of which are unconstrainable without knowing significantly more about the galaxy-absorber pair.

We emphasise that a proximity zone fossil can enhance metal lines over a significant path length if the AGN was strong in the past. We showed that a wide range of AGN intensities, as would be expected along a large path length through a proximity zone, will lead to similar recombination time histories and hence similar enhanced columns for high-ionisation species at a given density. If a proximity zone is many Mpc in size, then enhanced metal columns should be observed along a similar path length. A fossil zone could be traced by unusually strong high-ionisation species over a large velocity range as in the case of the Ne VIII in the Tripp et al. (2011) absorber, which extends over 1500 km s<sup>-1</sup>. This corresponds to a Hubble flow of over 10 proper Mpc implying an extended fossil zone and a very strong AGN in the past.

In summary, we propose a new time-dependent model for the  $z = 0.927$  PG1206+459 absorber that relies on en-

hanced photo-ionisation of  $T \sim 10^4$  K gas from either an AGN that turned off tens of Myr ago or an AGN that recently turned on. While our model can reproduce the columns of many of the higher ionisation lines, including Ne VIII, it requires a multi-phase structure with absorption by lower ionisation states, especially Mg II arising in much denser gas remaining shielded from the AGN. This scenario provides an alternative to the outflow shell model proposed by Tripp et al. (2011) of a  $T > 10^5$  K hot gas component and a velocity-coincident cold gas component, which may be expected for a propagating shock with post-shock radiatively cooling metal-enriched gas. Our AGN model requires a much smaller mass for high-ionisation components, as little as  $3 \times 10^7 M_{\odot}$  of gas, assuming a path through the centre of a spherical  $r \sim 14.5$  kpc, solar-enriched cloud with  $n_{\text{H}} \sim 10^{-3.5} \text{ cm}^{-3}$ .

### 3.2 AGN and proximity zone fossils at the peak of QSO activity at $z = 2.5$

Another application of our code is the transverse proximity effect (TPE) where a foreground QSO ionises gas along the sight line toward a background QSO. Recent work has been performed by Hennawi et al. (2006), Worseck & Wisotzki (2006); Worseck et al. (2007), and Gonçalves et al. (2008) who explored the TPE at  $z \sim 2.5$ , near the peak of QSO activity. The TPE can be elusive when traced by H I alone owing to complicating effects of the overdense regions creating more H I absorption, which goes in the opposite direction of decreased H I owing to the QSO ionisation (see also Schirber et al. 2004). For example, Hennawi & Prochaska (2007) argue that QSO emission is anisotropic based on the enhancement of Lyman-limit systems in transverse sight lines indicating that the QSO radiation does not effect off-sight line directions as often, even after accounting for the fact that QSOs may live in overdense regions.

Gonçalves et al. (2008) analysed metal-line systems in a quasar triplet at  $z \sim 2.5$  and found that the TPE was apparent when C IV and O VI aligned with H I are included in the analysis. They in fact argued that unusual  $N_{\text{OVI}}/N_{\text{HI}}$  and  $N_{\text{CIV}}/N_{\text{HI}}$  ratios of components in transverse proximity zones indicate that the QSO radiation field reaches off-sight line directions, and that the two foreground QSOs, which are extremely bright and rare, more likely radiate isotropically. Their work shows that the non-linear ionisation properties of metal lines, when used in conjunction with H I, can help constrain the TPE (see also Worseck & Wisotzki 2006; Worseck et al. 2007).

#### 3.2.1 The QSO-on phase

We turn on our AGN template spectrum for 20 Myr and find the average change in column density owing to the enhanced field. The left tables in Figure 7 show, from top to bottom, the average enhancement in H I, C IV, N V, and O VI of the time-averaged column densities during the 20 Myr QSO-on phase for a grid of densities ( $\log[n_{\text{H}}/\text{cm}^{-3}]$ ) and fluxes ( $\log[J_{\text{LL, equ}}/(\text{erg s}^{-1} \text{ cm}^{-2} \text{ Hz}^{-1} \text{ sr}^{-1})]$ ). The second column in each table shows equilibrium column densities ( $\log[N/\text{cm}^{-2}]$ ) using the HM01  $z = 2.5$  EGB, absorber lengths according to Schaye (2001), and solar metallicity. As

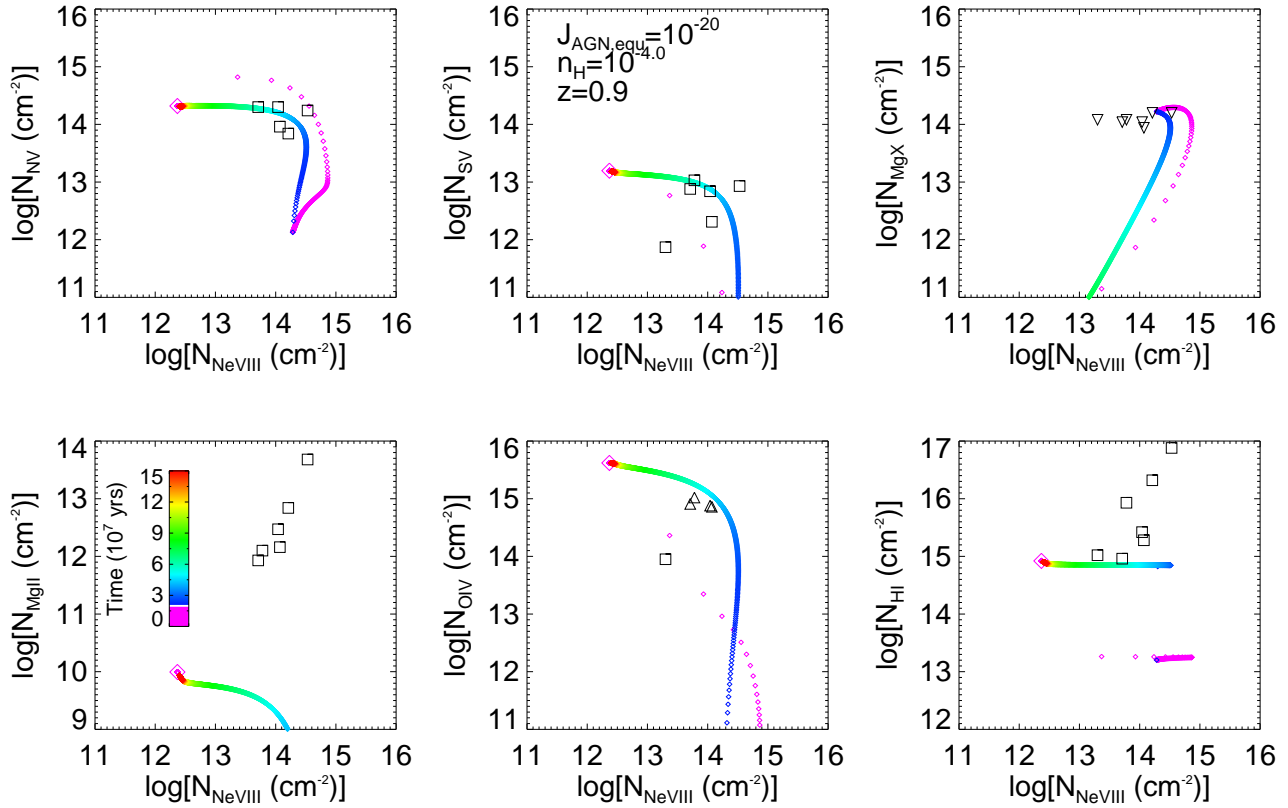


**Figure 6.** Column densities of observed species in the PG1206+459  $z = 0.927$  absorber by Tripp et al. (2011) (black squares are observed detections, triangles lower limits, upside down triangles upper limits) compared to the evolution of column densities predicted for the case shown in Figure 2:  $n_{\text{H}} = 10^{-4} \text{ cm}^{-3}$ ,  $T = 10^{4.2} \text{ K}$ ,  $l = 52 \text{ kpc}$ , solar metallicity with an AGN with intensity  $J_{\text{LL, equ}} = 10^{-20} \text{ erg s}^{-1} \text{ cm}^{-2} \text{ Hz}^{-1} \text{ sr}^{-1} \text{ cm}^{-2}$  turning on at  $t = 0$  and off at  $t = 20 \text{ Myr}$  after which the radiation field returns to the ever present  $z = 0.9$  HM01 EGB. N V, S V, Mg X, Mg II, O IV, and H I are plotted against Ne VIII in different panels from upper left to bottom right. Time  $t = 0$  is shown as the large magenta diamond, and small diamonds are plotted every  $10^5 \text{ yr}$ , colour-coded by age with the AGN-on phase being coloured magenta. The white line in the colour bar indicates when the AGN turns off and is obvious in the inflection point in the N V and Mg X plots. This model can approximately reproduce observations of Ne VIII, N V, S V, Mg X, and O IV at  $\sim 50 \text{ Myr}$  (30 Myr after the AGN turns off), but severely underestimates Mg II and also H I.

with all cases in this paper, we assume the gas initially rests at the temperatures where photo-heating balances cooling for the HM01 field, which fall from  $10^{4.68} \rightarrow 10^{4.07} \text{ K}$  as density increases from  $n_{\text{H}} = 10^{-5} \rightarrow 10^{-3} \text{ cm}^{-3}$  at  $z = 2.5$ . The grid cells to the right of the HM01 column indicate the column density change  $\delta \log[N]$  (in dex) relative to the HM01 equilibrium, colour-coded to be redder if the QSO decreases the column and bluer if it is increased.

The behaviour of H I is relatively easy to understand. As the AGN turns on,  $N_{\text{HI}}$  equilibrates to a column density that is inversely proportional to the intensity of the new radiation field. We define the AGN enhancement factor as

$$g_{\text{AGN}} = \frac{J_{\text{EGB}} + J_{\text{AGN, equ}}}{J_{\text{EGB}}}. \quad (6)$$

With the  $z = 2.5$  HM01 EGB having  $\log[J_{\text{LL}}] = -21.3$  combined with the weakest AGN field  $\log[J_{\text{LL, equ}}] = -21.5$ , H I is reduced by  $\log[g_{\text{AGN}}] = 0.2$  dex. The six AGN field enhancements we list range from  $g_{\text{AGN}} = 1.6$ -200, which decrease  $N_{\text{HI}}$  in the same proportion modulo the effect of photo-heating raising the temperature of the gas and thus further reducing H I. Photo-heating by the strongest AGN reduces H I by an additional factor of two in  $n_{\text{H}} = 10^{-3} \text{ cm}^{-3}$  gas, owing to the ejection of energetic metal electrons at X-ray energies.

The behaviour of the metal lines is not as simple as that of H I. As we saw in the previous subsection, AGN almost always ionise C IV to higher states and thus reduce their columns, while enhancing O VI at higher  $n_{\text{H}}$  and reducing it at lower  $n_{\text{H}}$ , depending on the field strength. We again assumed solar metallicity, but the listed  $\delta \log[N]$  values are applicable to other metallicities modulo the effect of increased photo-heating at higher metallicity. The same trends are observed by Gonçalves et al. (2008): increased O VI and decreased C IV. Their  $g_{\text{AGN}}$  ranged from 10 – 200 and they derived densities of  $n_{\text{H}} = 10^{-4.1} - 10^{-2.7} \text{ cm}^{-3}$ , which would correspond to the bottom three rows and right-most four columns in the left tables of Figure 7. One difference is that they use a single power law of  $\nu^{-1.8}$  in their UV EGB, while we are using the HM01 field enhanced with a  $\nu^{-1.57}$  AGN spectrum plus an X-ray component. This allows our field to ionise O VI to O VII and above, which explains why we find more reduction in  $N_{\text{OVI}}$  for the stronger fields: O VI is ionised to higher states much more easily.

An additional point about the TPE during the AGN-on phase is that O VI increases significantly more than H I decreases at higher densities and lower field strengths (see blue cells in bottom left panel of Figure 7). We may thus ex-

Average HI column during 20 Myr AGN-on phase								Average HI column during 20 Myr <i>following</i> AGN-on phase							
$\log[n_{\text{H}}]$	HM01	-21.5	-21.0	-20.5	-20.0	-19.5	-19.0	$\log[n_{\text{H}}]$	HM01	-21.5	-21.0	-20.5	-20.0	-19.5	-19.0
-5.0	12.7	-0.2	-0.5	-0.9	-1.3	-1.8	-2.3	-5.0	12.7	-0.0	-0.0	-0.0	-0.0	-0.0	-0.0
-4.5	13.6	-0.2	-0.5	-0.9	-1.3	-1.8	-2.3	-4.5	13.6	-0.0	-0.0	-0.0	-0.0	-0.0	-0.1
-4.0	14.5	-0.2	-0.5	-0.9	-1.4	-1.9	-2.4	-4.0	14.5	-0.0	-0.0	-0.0	-0.1	-0.1	-0.1
-3.5	15.4	-0.2	-0.5	-0.9	-1.4	-1.9	-2.4	-3.5	15.4	-0.0	-0.1	-0.1	-0.1	-0.2	-0.2
-3.0	16.2	-0.3	-0.6	-1.0	-1.5	-2.0	-2.5	-3.0	16.2	-0.0	-0.1	-0.1	-0.1	-0.2	-0.2

Average CIV column during 20 Myr AGN-on phase								Average CIV column during 20 Myr <i>following</i> AGN-on phase							
$\log[n_{\text{H}}]$	HM01	-21.5	-21.0	-20.5	-20.0	-19.5	-19.0	$\log[n_{\text{H}}]$	HM01	-21.5	-21.0	-20.5	-20.0	-19.5	-19.0
-5.0	11.9	-0.6	-1.1	-1.6	-2.2	-2.8	-3.3	-5.0	11.9	-0.4	-0.6	-1.2	-2.0	-2.4	-2.5
-4.5	13.6	-0.6	-1.0	-1.6	-2.2	-2.7	-3.3	-4.5	13.6	-0.4	-0.6	-1.1	-1.7	-2.0	-2.2
-4.0	14.8	-0.5	-1.0	-1.5	-2.1	-2.7	-3.3	-4.0	14.8	-0.3	-0.5	-0.8	-1.2	-1.4	-1.6
-3.5	15.4	-0.3	-0.8	-1.3	-1.9	-2.6	-3.1	-3.5	15.4	-0.2	-0.3	-0.4	-0.6	-0.8	-0.9
-3.0	15.6	+0.0	-0.3	-0.8	-1.4	-2.2	-2.8	-3.0	15.6	-0.0	-0.0	-0.1	-0.1	-0.2	-0.3

Average NV column during 20 Myr AGN-on phase								Average NV column during 20 Myr <i>following</i> AGN-on phase							
$\log[n_{\text{H}}]$	HM01	-21.5	-21.0	-20.5	-20.0	-19.5	-19.0	$\log[n_{\text{H}}]$	HM01	-21.5	-21.0	-20.5	-20.0	-19.5	-19.0
-5.0	12.4	-0.3	-0.7	-1.2	-1.7	-2.2	-2.8	-5.0	12.4	-0.3	-0.6	-1.0	-1.8	-2.6	-2.8
-4.5	13.7	-0.2	-0.6	-1.1	-1.6	-2.1	-2.7	-4.5	13.7	-0.3	-0.5	-0.9	-1.4	-2.0	-2.2
-4.0	14.4	-0.0	-0.3	-0.8	-1.4	-1.9	-2.5	-4.0	14.4	-0.1	-0.3	-0.5	-0.8	-1.1	-1.3
-3.5	14.6	+0.3	+0.2	-0.2	-0.8	-1.4	-2.1	-3.5	14.6	+0.1	+0.1	+0.0	-0.1	-0.2	-0.4
-3.0	14.3	+0.7	+0.9	+0.7	+0.2	-0.5	-1.3	-3.0	14.3	+0.1	+0.2	+0.3	+0.3	+0.2	+0.1

Average OVI column during 20 Myr AGN-on phase								Average OVI column during 20 Myr <i>following</i> AGN-on phase							
$\log[n_{\text{H}}]$	HM01	-21.5	-21.0	-20.5	-20.0	-19.5	-19.0	$\log[n_{\text{H}}]$	HM01	-21.5	-21.0	-20.5	-20.0	-19.5	-19.0
-5.0	13.8	-0.1	-0.3	-0.8	-1.3	-1.8	-2.3	-5.0	13.8	-0.2	-0.5	-0.9	-1.5	-2.5	-2.9
-4.5	14.9	+0.0	-0.2	-0.6	-1.2	-1.7	-2.2	-4.5	14.9	-0.1	-0.3	-0.6	-1.1	-1.7	-2.0
-4.0	15.2	+0.2	+0.1	-0.2	-0.8	-1.3	-1.9	-4.0	15.2	+0.1	+0.0	-0.1	-0.3	-0.6	-0.8
-3.5	14.9	+0.6	+0.8	+0.6	+0.1	-0.5	-1.2	-3.5	14.9	+0.3	+0.4	+0.4	+0.4	+0.3	+0.2
-3.0	14.4	+0.9	+1.4	+1.5	+1.3	+0.8	-0.0	-3.0	14.4	+0.2	+0.5	+0.7	+0.7	+0.7	+0.6

**Figure 7.** Time-averaged column densities of H I (top panels), C IV (2nd panels), N V (3rd panels) and O VI (bottom panels) for a  $z = 2.5$  AGN-on phase lasting 20 Myr (left panels) and the fossil effect of the 20 Myr immediately after the AGN turns off (right panels). The 2nd column lists  $\log[N/\text{cm}^{-2}]$  for the normal HM01 EGB at  $z = 0.25$ , assuming ionisation equilibrium and solar metallicity, for 5 different densities (listed as  $\log[(\text{cm}^{-3})]$  in 1st column). The remaining columns indicate the effect of the AGN intensities (listed in the 2nd row in  $\log[J_{\text{LL, equ}}]$  units, where  $\log[J_{\text{LL, equ}}] = -21.3$  at  $z = 2.5$  for the HM01 EGB) shown by the increase or decrease in  $\log[N]$  relative to the HM01  $\log[N]$ . Cell colour indicates whether the AGN increased (bluer) or decreased (redder) the column density. H I is heavily affected during the AGN-on phase, but returns to nearly the original column afterwards. C IV, N V, and O VI are also strongly affected during the AGN-on phase, and show time-averaged columns over the next 20 Myr that remain out of equilibrium. Solar metallicity is assumed, but the metal columns scale with metallicity, except for the minor effect of AGN photo-heating raising the temperature slightly.

pect significantly enhanced O VI with weaker than usual H I toward the edge of a proximity zone, which may approach  $\sim 10$  proper Mpc in size for the brightest QSOs. In fact, the large enhancement in proximate O VI absorbers observed by Tripp et al. (2008) within  $1500 \text{ km s}^{-1}$  of the brightest QSOs at lower redshifts (or  $\sim 17$  Mpc at  $z = 0.5$ ), combined with their lower observed  $N_{\text{HI}}/N_{\text{OVI}}$  ratios agrees with this prediction. We put forth a model that these are not absorbers

directly associated with the QSOs, but instead intervening IGM absorbers on the outskirts of the proximity zone with a  $g_{\text{AGN}}$  of a few and perhaps even less than two. This of course assumes that the AGN has a harder EUV spectrum than the EGB.

A similar point can be made that N V could be enhanced in AGN proximity zones. Only cells with  $n_{\text{H}} = 10^{-3.0} \text{ cm}^{-3}$  and weaker AGN fields show noticeably enhanced N V when

the AGN is on, but these cells may be well-represented in QSO proximity zones. Consider that while  $N_{\text{NV}}$  for the equilibrium HM01 field peaks at  $n_{\text{H}} = 10^{-3.5} \text{ cm}^{-3}$  (assuming  $Z_{\odot}$  as in Figure 7), the highest observed NV column may correspond to  $n_{\text{H}} = 10^{-3.0}$  given that metallicity likely correlates with density. Factoring in that most of the proximate volume and path length corresponds to the weaker fields, the strongest observable NV columns could correspond to the outskirts of proximity zones. Since nitrogen is less abundant than other metals and NV is much rarer than CIV and OVI, this AGN enhancement could boost normally unobservable or hard-to-detect NV columns by  $\sim 5 - 10\times$  into obvious detections.

### 3.2.2 QSO proximity zone fossils

We now cross over to the fossil phase by considering the time-averaged columns of HI and metals during the first 20 Myr after the QSO turns off. This timescale is chosen to demonstrate that significant fossil effects can persist on a similar timescale as  $\tau_{\text{AGN}}$ . We show the deviations in columns on the right side of Figure 7. Listed is the time-averaged column deviation over this time span (note that the actual deviation will likely be larger or smaller at a specific fossil zone time).

The CIV column is almost always reduced, but not to the same extent as during the QSO-on phase. Nonetheless, if a significant fraction of intervening CIV absorbers reside in fossil zones, then models that try to fit these assuming a uniform EGB like HM01 (e.g. Schaye et al. 2003; Simcoe et al. 2004; Oppenheimer & Davé 2006; Tescari et al. 2011) would underestimate the amount of carbon. Hence, the true global ionisation correction of CIV would be larger, and the inferred IGM metallicity would be too low. The opposite would be true for OVI at higher densities, but it would have the same trend as CIV if it mostly arises from lower density gas. Meanwhile, HI would remain nearly unaffected except for the slightly reduced columns owing to photo-heating of metals. The resulting absorption line systems will have ratios (e.g. OVI/HI and CIV/HI) that would differ significantly from those predicted by equilibrium models with a normal EGB or in a proximity zone.

### 3.2.3 How affected are metal lines by fluctuating AGN?

We now present an estimate of the fraction of the volume of the Universe that may be affected by transverse AGN proximity and fossil zones at high- $z$ . We estimate the luminosity function ( $\Phi(L_{\nu}, \#/\text{Mpc}^{-3}/\log(L_{\nu}))$ ) of AGN at 912Å using the analytic fitting formulae of Hopkins et al. (2007) at  $z = 2.5^2$ . For a given isolated AGN, the proper radius within which the AGN flux is at least  $g_{\text{AGN}} - 1$  times  $J_{\nu}$  is given by  $R = \sqrt{L_{\nu}/((4\pi)^2(g_{\text{AGN}} - 1)J_{\nu})}$ , where  $L_{\nu}$  is the AGN luminosity at  $\nu$  in  $\text{ergs s}^{-1} \text{ Hz}^{-1}$ . Hence, the fractional volume,

$V_{\text{AGN}}$ , exposed to at least  $g_{\text{AGN}} - 1$  is

$$V_{\text{AGN}} = \int \phi(L_{\nu}) \frac{4\pi}{3} \left( \frac{L_{\nu}}{(4\pi)^2(g_{\text{AGN}} - 1)J_{\nu}} \right)^{3/2} (1+z)^3 dL_{\nu} \quad (7)$$

when integrating over the luminosity function ( $\nu$  is in the rest frame). The  $(1+z)^3$  term is a result of  $\Phi(L_{\nu})$  being in comoving Mpc and our proximity zone units being proper units. Using  $J_{\nu} = 10^{-21.3} \text{ erg s}^{-1} \text{ cm}^{-2} \text{ Hz}^{-1} \text{ sr}^{-1}$  at  $z = 2.5$ , the volume ionised by AGN to at least the level of the HM01 background,  $g_{\text{AGN}} = 2$ , is 0.16%, and the volume ionised to  $g_{\text{AGN}} = 10$  is 0.005%. This calculation does not depend on how anisotropically AGN emit, because the average subtended solid angle over which AGN of a given luminosity emit is compensated by the number of all emitting AGN for that luminosity. The  $V_{\text{AGN}}$  fractions are much lower at lower redshift, where AGN are less frequent and the Universe has expanded.

While the fraction of volume with  $g_{\text{AGN}} \geq 2$  is small compared to the volume filling factors of metals in simulations calibrated to fit observed CIV statistics, which is of order 10% at  $z \sim 2 - 3$  (Oppenheimer & Davé 2006; Booth et al. 2012), there are reasons to argue that AGN proximity and fossil zones could affect a significant fraction of observed metal lines. First, strong CIV systems ( $N_{\text{CIV}} \gtrsim 10^{14} \text{ cm}^{-3}$ ) are associated with Lyman-break galaxies (LBGs) at small radii (80-85 proper kpc Adelberger et al. 2005; Steidel et al. 2010), and the co-moving line density of such strong absorbers is consistent with being within 50 kpc of  $\geq 0.5L^*$  LBGs (Cooksey et al. 2012). This implies that many of the strongest metal-line absorbers occupy the small fraction of volume with enhanced ionisation.

More importantly, the multiplicative effects of AGN with short duty cycles can significantly expand the volume affected by fossil zones. Our lower redshift example in Figure 5 shows that a  $d = 4\%$  duty cycle leads to  $3\times$  greater OVI and  $5\times$  reduced CIV columns time-averaged once the AGN first turns on at  $t = 0$ . This duty cycle is relevant since the observed fraction of LBGs with active AGN is  $\sim 3\%$  (Steidel et al. 2002), which could reflect their duty cycle. Taking  $1/d$  for  $d = 4\%$  means that the fossil effect applies to a  $25\times$  greater volume than the proximity zone effect, and hence that 4% of the total volume is affected by  $g_{\text{AGN}} \geq 2$ . This volume fraction is similar to that thought to be required to account for the observed incidence of weak metal lines (Oppenheimer & Davé 2006; Booth et al. 2012) suggesting that non-equilibrium AGN fossil zones may be critically important. Finally, metal lines can be enhanced if  $g_{\text{AGN}} < 2$ , as is shown in Figure 7 for  $\log[J_{\text{LL,eq}}] = -21.5$ , or  $g_{\text{AGN}} = 1.6$ . This leads to a doubling of the volume affected by both proximity and fossil zones, and CIV is reduced by  $2 - 4\times$  in almost every case. Again, this arises because the AGN EUV spectrum is harder than that of the EGB.

We conclude that a large fraction of metal lines could arise from fossil zones at high- $z$ , but precisely what fraction depends on many factors. If the AGN-on phase is long-lived and singular for most AGN then the fossil effect would be limited. However, if AGN are fluctuating with short duty cycles in typical star-forming galaxy hosts and have hard EUV slopes, then the fossil effect could be a critical consideration for typical metal lines. We may have to re-evaluate the phys-

<sup>2</sup> We used their script at <http://www.cfa.harvard.edu/~phopkins/Site/qlf.html>.

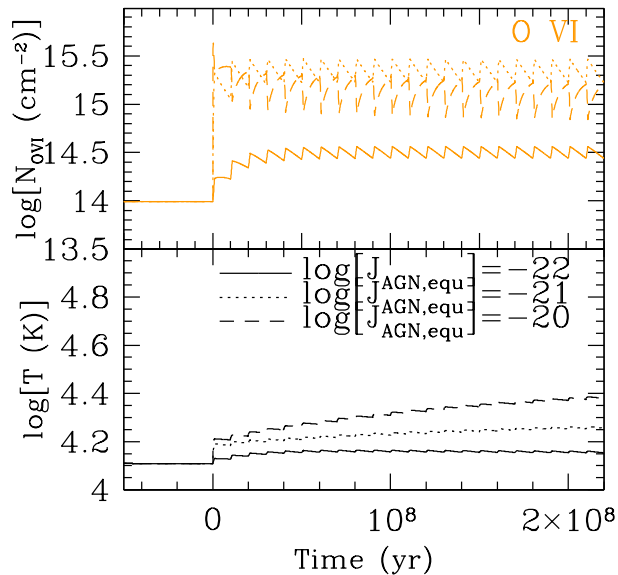


**Figure 8.** The time evolution of O VI columns (top panel) and gas temperature (bottom panel) for a  $n_{\text{H}} = 10^{-4} \text{cm}^{-3}$ ,  $l = 52$  kpc solar metallicity absorber at  $z = 0.25$ , where an AGN of the listed intensity turns on for 1 Myr every 10 Myr starting at  $t = 0$ . The periodic AGN activity significantly enhances O VI columns and doubles the gas temperature over 200 Myr in the most extreme case via photo-heating of metals. This case could be applicable for metals around normal looking galaxies if AGN duty cycles are short and have frequencies comparable to the O VI recombination timescale.

ical interpretation of C IV and O VI absorbers at high- $z$ , and the amount of underlying metals traced in diffuse gas.

### 3.3 Low-redshift Seyferts ionising their circumgalactic media

Our last case study are low-redshift metal absorbers associated with weaker AGN, such as Seyferts. We consider an admittedly idealised situation of a 10% duty cycle where the AGN turns on for 1 Myr out of every 10 Myr at  $z = 0.25$ . We plot the time history of O VI in Figure 8 for three different field enhancements, to show how the continuous pumping resulting from a short duty cycle can even significantly enhance the ionisation around weak AGNs. We again assume  $n_{\text{H}} = 10^{-4} \text{cm}^{-3}$  solar-enriched gas at the equilibrium temperature of  $T = 10^{4.1}$  K.

This situation may be applicable to Markarian galaxies in the local Universe. These are among the biggest, brightest spirals, and have an unusually blue central core that usually requires non-thermal emission, which often indicates AGN activity. About 10% of Markarians are Seyferts (Weedman 1977), which motivates our choice of a 10% duty cycle. Of course, not all Markarians are Seyferts with a short duty cycle, but we consider the possibility that  $\sim 10\%$  of Markarians were more active AGNs in the recent past (i.e. in the last  $\sim 10$  Myr). The three cases plotted in Figure 8,  $J_{\text{LL, equ}} = 10^{-22.0}$ ,  $10^{-21.0}$ , and  $10^{-20.0} \text{erg s}^{-1} \text{cm}^{-2} \text{Hz}^{-1} \text{sr}^{-1}$  correspond to soft X-ray luminosities at 100 proper kpc of

$L_{0.5-2.0} = 10^{42.1}$ ,  $10^{43.1}$ , and  $10^{44.1} \text{erg s}^{-1}$  AGN, respectively, using our AGN template spectrum. These luminosities are in the range of Seyfert X-ray luminosities observed by Rush et al. (1996). The bottom panel of Figure 8 shows that the temperature doubles to  $10^{4.4}$  K in the strongest case.

We tabulate the time-averaged enhancements of C IV, O VI, and Ne VIII over 200 Myr, or the first 20 cycles, for a grid of densities ( $\log[n_{\text{H}}/\text{cm}^{-3}]$ ) and AGN fluxes ( $\log[J_{\text{LL, equ}}/(\text{erg s}^{-1} \text{cm}^{-2} \text{Hz}^{-1} \text{sr}^{-1})]$ ) in Figure 9. Similar to Figure 7, the second column in each table shows column densities ( $\log[N/\text{cm}^{-2}]$ ) using the HM01 EGB (here at  $z = 0.25$ ), absorber lengths according to Schaye (2001),  $T = 10^{3.85-4.40}$  K before the AGN turns on, and solar metallicity. The grid cells to the right indicate the column density change  $\delta \log[N]$  relative to the HM01 equilibrium, colour-coded to be redder if the column density goes down due to the AGN and bluer if it goes up. The  $n_{\text{H}}$  densities correspond to overdensities ranging from 27 to 2700. While we show solar metallicity, the change is similar for lower metallicities.

The main point of this diagram is to show that even for a 10% AGN duty cycle, the time-averaged columns are significantly changed, mostly in a positive direction for these higher metal ions. While there has never been a survey designed to probe the halos of galaxies showing signs of ongoing or recent AGN activity in the low-redshift Universe, it may be worth exploring in light of the COS observations of Tumlinson et al (2011) revealing very strong O VI around normal spiral, star-forming galaxies at  $z \sim 0.2$ . Markarian galaxies, for example, may show even stronger O VI if this gas originates from a photo-ionised component at  $T < 10^5$  K.

## 4 SUMMARY

The assumption of a uniform extra-galactic background breaks down in an AGN proximity zone, which is over-ionised relative to the rest of the IGM. H I columns are reduced and metals are ionised to higher states owing to increased ionisation. We demonstrate here that once the AGN turns off, metals residing in “fossil” AGN proximity zones may be over-ionised for timescales exceeding the typical AGN-on phase. Using the non-equilibrium code introduced in Oppenheimer & Schaye (2013), we follow metal-enriched gases initially ionised by the extra-galactic ionisation background (Haardt & Madau 2001) under the effect of increased ionisation from a local AGN. After the AGN turns off, metal ions in fossil proximity zones often require many Myr to return to the equilibrium values, owing to significant recombination times of metal ion species. We demonstrate how this non-equilibrium fossil effect alters observational metal-line diagnostics used to constrain the physical state of intergalactic and circum-galactic gas. In particular, we show that commonly observed Lithium-like ions (i.e. C IV, N V, O VI, Ne VIII) can be heavily affected at a range of redshifts from the present-day to  $z \gg 3$ . This behaviour is in contrast to H I, which re-equilibrates comparatively rapidly once an AGN turns off, owing to its equilibrium state having very low neutral fractions in the IGM.

We consider metal-enriched gas with densities  $n_{\text{H}} =$

Average CIV column with an AGN on 10% of the time							
$\log[n_{\text{H}}]$	HM01	-22.5	-22.0	-21.5	-21.0	-20.5	-20.0
-5.0	14.0	-0.0	-0.1	-0.4	-0.9	-1.6	-2.2
-4.5	14.7	+0.0	-0.0	-0.2	-0.7	-1.2	-1.7
-4.0	14.9	+0.1	+0.2	+0.2	-0.1	-0.5	-0.8
-3.5	14.6	+0.2	+0.4	+0.6	+0.6	+0.4	+0.2
-3.0	14.2	+0.2	+0.5	+0.9	+1.0	+1.0	+0.9

Average OVI column with an AGN on 10% of the time							
$\log[n_{\text{H}}]$	HM01	-22.5	-22.0	-21.5	-21.0	-20.5	-20.0
-5.0	14.7	+0.0	+0.1	+0.1	+0.0	-0.4	-1.0
-4.5	14.6	+0.1	+0.3	+0.5	+0.6	+0.4	-0.1
-4.0	14.0	+0.2	+0.5	+0.9	+1.3	+1.4	+1.2
-3.5	13.2	+0.3	+0.7	+1.3	+1.9	+2.3	+2.3
-3.0	12.2	+0.4	+1.0	+1.8	+2.6	+3.1	+3.3

Average NeVIII column with an AGN on 10% of the time							
$\log[n_{\text{H}}]$	HM01	-22.5	-22.0	-21.5	-21.0	-20.5	-20.0
-5.0	13.4	+0.1	+0.2	+0.4	+0.7	+0.8	+0.6
-4.5	12.3	+0.2	+0.4	+0.9	+1.5	+2.0	+2.1
-4.0	10.8	+0.3	+0.7	+1.4	+2.3	+3.2	+3.7
-3.5	9.0	+0.4	+1.1	+2.1	+3.4	+4.6	+5.3
-3.0	7.2	+0.6	+1.7	+3.1	+4.6	+5.9	+6.8

**Figure 9.** Time-averaged column densities of CIV (top panel), OVI (middle panel), and NeVIII (lower panel) assuming that a  $z = 0.25$  AGN turns on for 1 Myr every 10 Myr. The 2nd column lists  $\log[N \text{ (cm}^{-2}\text{)}]$  for the normal HM01 field at  $z = 0.25$ , assuming solar metallicity, for 5 different  $n_{\text{H}}$  densities (listed as  $\log[(\text{cm}^{-3})]$  in the 1st column). The rest of the columns indicate the time averaged effect of the AGN intensities (listed in the 2nd row in  $\log[J_{\text{LL,equ}}]$  where  $\log[J_{\text{LL,equ}}] = -22.2$  at  $z = 0.25$  for the HM01 EGB) shown by the relative increase or decrease in  $\log[N]$  relative to the HM01  $\log[N]$ . Cell colour indicates whether the AGN increases (blue) or decreases (red) the column density. Despite the AGN being on only 10% of the time, metal columns can be affected, mostly in a positive direction. Solar metallicity is assumed, but the metal columns scale with metallicity, except for the minor effect of AGN photo-heating raising the temperature slightly.

$10^{-5} - 10^{-3} \text{ cm}^{-3}$  at  $z = 2.5, 0.9$  and  $0.25$ , which corresponds to diffuse IGM and CGM gas, that is initially in thermal equilibrium ( $T \sim 10^4 - 10^{4.5}$  K). Our parameter choices are based on hydrodynamic simulations showing a significant fraction of diffuse metals in thermal equilibrium, where cooling balances photo-heating, owing to short cooling times from higher temperatures ( $T \sim 10^5 - 10^6$  K). The gas begins in ionisation equilibrium with the HM01 EGB, and becomes irradiated by an AGN template spectrum turned on for 1 to 20 Myr corresponding to an ionisation increase of between  $1.6 - 500\times$  the EGB radiation field strength at the Lyman limit.

Our fiducial case corresponds to a local AGN turning

on at  $z = 0.9$  where a wide range of metal lines are observable with current facilities (e.g. COS on HST) and inspired by the Tripp et al. (2011) observations of very strong Ne VIII absorption in a system associated with a galaxy exhibiting post-starburst and possible AGN signatures. We show that for reasonable AGN energies, Ne VIII columns are increased by a factor of  $\sim 100$  during a 20 Myr AGN-on phase and also the 15 Myr in the following fossil phase, and remain  $> 10\times$  stronger for 50 Myr after. We show for a variety of gas densities, AGN strengths, and AGN lifetimes that Ne VIII columns of  $10^{14} - 10^{15} \text{ cm}^{-3}$  are possible for significant timescales during the fossil phase for solar abundances. We directly model the components of the Tripp et al. (2011) absorber, finding that a model with  $T < 10^5$  K gas in a fossil zone of 10-30 Myr can reproduce many of the observed columns and upper limits using as little as  $3 \times 10^7 M_{\odot}$  of solar enriched gas per component. Solutions are also possible if the AGN is currently on. However, a separate phase is necessary for all solutions to explain the Mg II and strong H I columns. Our application to this absorption system demonstrates that a whole new class of non-equilibrium solutions are available for metal-enriched diffuse gas in the presence of evolving ionisation fields.

We also model AGN ionisation at  $z \sim 2.5$ , including the transverse proximity effect for a foreground QSO zone in a QSO pair, where observed CIV/H I and OVI/H I line ratios indicate enhanced ionisation over the normal EGB (Gonçalves et al. 2008). We first show that active proximity zones can exhibit these unique ratios, and then consider how the non-equilibrium fossil effect can alter CIV and OVI columns for timescales longer than the AGN lifetime. Unique line ratios are possible where H I has rapidly re-equilibrated but the metal lines are still recombining. We argue that it is possible that fossil zones could affect many more absorbers in the high- $z$  Universe than AGN proximity zones if AGNs fluctuate with short duty cycles, have hard extreme UV slopes, and are associated with typical star-forming galaxies, which prolifically enrich the IGM. A large fraction of intervening metal absorbers in typical QSO spectra could be affected by the fossil effect, meaning that ionisation corrections assuming a uniform EGB would be wrong. CIV columns are almost always reduced in fossils meaning that the true diffuse gas metallicity becomes higher than when one assumes equilibrium with the EGB field.

Finally, we consider lower redshift AGN ionising their surrounding CGM with a 10% duty cycle where the AGN is on for 1 out of every 10 Myr. Despite this short duty cycle, high ions (OVI and NeVIII) are significantly enhanced often by more than 1 dex, and temperatures are increased by a factor of two for stronger fields. The key to these increases of metal columns and temperature are that the photo-ionisation/photo-heating timescales are short or comparable to the AGN lifetime, and the recombination/cooling timescale is long or comparable to the duty cycle interval. The result is intriguing in that surprisingly little energy input is necessary to greatly enhance metal columns in the halo of fluctuating typical AGN.

These non-equilibrium fossil and proximity zone effects may complicate the analysis of intergalactic metal lines that assume photo-ionisation equilibrium with a uniform EGB. The fossil effect is unique in that H I re-equilibrates rapidly while metal lines remain over-ionised leading to different

ionisation corrections to obtain metallicities. This could be particularly important during the quasar era,  $z \sim 2 - 5$ , for which we find that the fraction of the volume occupied by fossil zones may be similar to the fraction that is thought to be enriched with heavy elements.

## ACKNOWLEDGEMENTS

We are grateful for discussions with Sebastiano Cantalupo, Arlin Crotts, Romeel Davé, Kristian Finlator, Martin Haehnelt, Zoltan Haiman, Phil Hopkins, Mike Shull, Chuck Steidel, Todd Tripp, and Lisa Winter. We thank Ali Rahmati for a thorough review of this manuscript. This work benefited from financial support from the Netherlands Organisation for Scientific Research (NWO) through VENI and VIDI grants, from NOVA, from the European Research Council under the European Union's Seventh Framework Programme (FP7/2007-2013) / ERC Grant agreement 278594-GasAroundGalaxies and from the Marie Curie Training Network CosmoComp (PITN-GA-2009-238356). We are also thankful for the hospitality provided by the University of Colorado, Boulder where part of this work was completed.

## REFERENCES

- Adelberger K. L., Shapley A. E., Steidel C. C., Pettini M., Erb D. K., & Reddy N. A. 2005, *ApJ*, 629, 636
- Aguirre, A., Dow-Hygelund, C., Schaye, J., & Theuns, T. 2008, *ApJ*, 689, 851
- Altay, G., Theuns, T., Schaye, J., Crighton, N. H. M., & Dalla Vecchia, C. 2011, *ApJL*, 737, L37
- Bajtlik, S., Duncan, R. C., & Ostriker, J. P. 1988, *ApJ*, 327, 570
- Bolton, J. S., & Haehnelt, M. G. 2007, *MNRAS*, 374, 493
- Booth, C. M., Schaye, J., Delgado, J. D., & Dalla Vecchia, C. 2012, *MNRAS*, 420, 1053
- Carswell, R. F., Webb, J. K., Baldwin, J. A., & Atwood, B. 1987, *ApJ*, 319, 709
- Cen, R., & Chisari, N. E. 2011, *ApJ*, 731, 11
- Cooksey, K. L., Kao, M. M., Simcoe, R. A., O'Meara, J. M., & Prochaska, J. X. 2012, *arXiv:1204.2827*
- Danforth, C. W. & Shull, M. J. 2008, *ApJ*, 679, 194
- Davé, R., Oppenheimer, B. D., Katz, N., Kollmeier, J. A., & Weinberg, D. H. 2010, *MNRAS*, 408, 2051
- Faucher-Giguère, C.-A., Lidz, A., Zaldarriaga, M., & Hernquist, L. 2009, *ApJ*, 703, 1416
- Ferland, G. J., Korista, K. T., Verner, D. A., Ferguson, J. W., Kingdon, J. B., & Verner, E. M. 1998, *PASP*, 110, 761
- Furlanetto, S. R., Haiman, Z., & Oh, S. P. 2008, *ApJ*, 686, 25
- Gonçalves, T. S., Steidel, C. C., & Pettini, M. 2008, *ApJ*, 676, 816
- Haardt, F. & Madau, P. 1996, *ApJ*, 461, 20
- Haardt, F. & Madau, P. 2001, in "Clusters of galaxies and the high redshift universe observed in X-rays, Recent results of XMM-Newton and Chandra", XXXVIth Rencontres de Moriond, eds. D.M. Neumann & J.T.T. Van
- Haiman, Z., & Hui, L. 2001, *ApJ*, 547, 27
- Hennawi, J. F., Prochaska, J. X., Burles, S., et al. 2006, *ApJ*, 651, 61
- Hennawi, J. F., & Prochaska, J. X. 2007, *ApJ*, 655, 735
- Hopkins, P. F., Hernquist, L., Cox, T. J., et al. 2006, *ApJS*, 163, 1
- Hopkins, P. F., Richards, G. T., & Hernquist, L. 2007, *ApJ*, 654, 731
- Jakobsen, P., Jansen, R. A., Wagner, S., & Reimers, D. 2003, *A&A*, 397, 891
- Lehner, N., Savage, B. D., Richter, P., Sembach, K. R., Tripp, T. M., & Wakker, B. P. 2007, *ApJ*, 658, 680
- Martini, P., & Weinberg, D. H. 2001, *ApJ*, 547, 12
- Muzahid, S., Srianand, R., Arav, N., Savage, B. D., & Narayanan, A. 2013, *arXiv:1302.5510*
- Narayanan, A., Wakker, B. P., & Savage, B. D. 2009, *ApJ*, 703, 74
- Narayanan, A., et al. 2011, *ApJ*, 730, 15
- Oppenheimer, B. D. & Davé, R. A. 2006, *MNRAS*, 373, 1265
- Oppenheimer, B. D. & Davé, R. A. 2009, *MNRAS*, 395, 1875
- Oppenheimer, B. D., Davé, R., Katz, N., Kollmeier, J. A., & Weinberg, D. H. 2012, *MNRAS*, 420, 829
- Oppenheimer, B. D., & Schaye, J. 2013, *arXiv:1302.5710*
- Péroux, C., Kulkarni, V. P., Meiring, J., et al. 2006, *A&A*, 450, 53
- Prochaska, J. X., Chen, H.-W., Howk, J. C., Weiner, B. J., & Mulchaey, J. 2004, *ApJ*, 617, 718
- Prochaska, J. X., O'Meara, J. M., Herbert-Fort, S., et al. 2006, *ApJL*, 648, L97
- Rahmati, A., Pawlik, A. H., Raičević, M., & Schaye, J. 2013, *MNRAS*, 765
- Rush, B., Malkan, M. A., Fink, H. H., & Voges, W. 1996, *ApJ*, 471, 190
- Savage, B. D., Lehner, N., Wakker, B. P., Sembach, K. R., & Tripp, T. M. 2005, *ApJ*, 626, 776
- Schaye, J. 2001, *ApJ*, 559, 507
- Schaye, J., Aguirre, A., Kim, T.-S., Theuns, T., Rauch, M., & Sargent, W.L.W. 2003, *ApJ*, 596, 768
- Schaye, J., Carswell, R. F., & Kim, T.-S. 2007, *MNRAS*, 379, 1169
- Schirber, M., Miralda-Escudé, J., & McDonald, P. 2004, *ApJ*, 610, 105
- Scott, J., Bechtold, J., Dobrzycki, A., & Kulkarni, V. P. 2000, *ApJS*, 130, 67
- Scott, J. E., Kriss, G. A., Brotherton, M., et al. 2004, *ApJ*, 615, 135
- Shull, J. M., Roberts, D., Giroux, M. L., Penton, S. V., & Fardal, M. A. 1999, *AJ*, 118, 1450
- Shull, J. M., France, K., Danforth, C. W., Smith, B., & Tumlinson, J. 2010, *ApJ*, 722, 1312
- Shull, J. M., Stevans, M., & Danforth, C. W. 2012, *ApJ*, 752, 162
- Simcoe, R. A., Sargent, W. L. W., & Rauch, M. 2004, *ApJ*, 606, 92
- Simcoe, R.A., Sargent, W.L.W., Rauch, M., & Becker, G. 2006, *ApJ*, 637, 648
- Smith, B. D., Hallman, E. J., Shull, J. M., & O'Shea, B. W. 2011, *ApJ*, 731, 6
- Steidel, C. C., Hunt, M. P., Shapley, A. E., et al. 2002, *ApJ*, 576, 653



- Steidel, C. C., Erb, D. K., Shapley, A. E., Pettini, M., Reddy, N., Bogosavljević, M., Rudie, G. C., & Rakic, O. 2010, *ApJ*, 717, 289
- Telfer, R. C., Kriss, G. A., Zheng, W., Davidsen, A. F., & Tytler, D. 2002, *ApJ*, 579, 500
- Tepper-García, T., Richter, P., Schaye, J., Booth, C. M., Dalla Vecchia, C., Theuns, T., & Wiersma, R. P. C. 2011, *MNRAS*, 413, 190
- Tepper-García, T., Richter, P., Schaye, J., Booth, C. M., Dalla Vecchia, C., & Theuns, T. 2012, *MNRAS*, 425, 1640
- Tescari, E., Viel, M., D’Odorico, V., Cristiani, S., Calura, F., Borgani, S., & Tornatore, L. 2011, *MNRAS*, 411, 826
- Thom, C. & Chen, H.-W. 2008b, *ApJS*, 179, 37
- Tilton, E. M., Danforth, C. W., Shull, J. M., & Ross, T. L. 2012, *ApJ*, 759, 112
- Tripp, T. M., Semback, K. R., Bowen, D. V., Savage, B. D., Jenkins, E. B., Lehner, N., & Richter, P. 2008, *ApJS*, 177, 39
- Tripp, T. M., Meiring, J. D., Prochaska, J. X., et al. 2011, *Science*, 334, 952
- Tumlinson, J., Thom, C., Werk, J. K., et al. 2011, *Science*, 334, 948
- Weedman, D. W. 1977, *ARA&A*, 15, 69
- Wiersma, R. P. C., Schaye, J., Dalla Vecchia, C., Booth, C. M., Theuns, T., & Aguirre, A. 2010, *MNRAS*, 409, 132
- Wiersma, R. P. C., Schaye, J., & Theuns, T. 2011, *MNRAS*, 415, 353
- Worseck, G., & Wisotzki, L. 2006, *A&A*, 450, 495
- Worseck, G., Fechner, C., Wisotzki, L., & Dall’Aglio, A. 2007, *A&A*, 473, 805
- Zuo, L. 1992, *MNRAS*, 258, 36